J. Fluid Mech. (1997), *vol.* 330, *pp.* 375–409

Sound generation in a mixing layer

By TIM COLONIUS[1], SANJIVA K. LELE[2]† AND PARVIZ MOIN[2]‡

[1]Division of Engineering and Applied Science, California Institute of Technology, Pasadena, CA 91125, USA

[2]Department of Mechanical Engineering, Stanford University, Stanford, CA 94305, USA

(Received 7 September 1995 and in revised form 22 August 1996)

The sound generated by vortex pairing in a two-dimensional compressible mixing layer is investigated. Direct numerical simulations (DNS) of the Navier–Stokes equations are used to compute both the near-field region and a portion of the acoustic field. The acoustic analogy due to Lilley (1974) is also solved with acoustic sources determined from the near-field data of the DNS. It is shown that several commonly made simplifications to the acoustic sources can lead to erroneous predictions for the acoustic field. Predictions based on the quadrupole form of the source terms derived by Goldstein (1976*a*, 1984) are in excellent agreement with the acoustic field from the DNS. However, despite the low Mach number of the flow, the acoustic far field generated by the vortex pairings cannot be described by considering compact quadrupole sources. The acoustic sources have the form of modulated wave packets and the acoustic far field is described by a superdirective model (Crighton & Huerre 1990). The presence of flow–acoustic interactions in the computed source terms causes the acoustic field predicted by the acoustic analogy to be very sensitive to small changes in the description of the source.

1. Introduction

Direct numerical simulation (DNS) of the unsteady Navier–Stokes equations is used to compute both the near field and a portion of the acoustic field of a plane mixing layer. The acoustic field is also determined by solving an acoustic analogy (Lilley 1974) with necessary source terms determined from the near-field data of the Navier–Stokes equations. This allows a detailed investigation of the acoustic sources associated with the flow and validates the acoustic analogy approach for a flow with an extensive vorticity field.

The mixing layer, consisting of two streams of fluid with unequal velocities, occurs in many natural, laboratory, and technological flows and serves as a model for the initial shear layer region of a jet. Large-scale coherent structures in mixing layers, such as those observed by Brown & Roshko (1974), have been extensively studied experimentally and computationally. Often the structures are initiated by forcing the flow at its fundamental (most unstable) frequency, f, or one of its subharmonics, $f/2$, $f/4$, etc. These frequencies are determined by linear stability analysis of the corresponding steady flow (usually an inviscid parallel flow.) The

† Also with Department of Aeronautics and Astronautics, Stanford University.
‡ Also with NASA Ames Research Center.

fundamental frequency excites instability waves which roll up into vortices which subsequently convect downstream. Subharmonic forcing causes adjacent vortices to pair further downstream. Such large-scale vortices and vortex pairings can also be present in jets.

Kibens (1980) measured the acoustic field of a high-speed round jet which was forced at its most unstable frequency and showed that the natural broad-band noise of the jet was suppressed, and the most significant sound was generated at the subharmonic frequencies. He identified the sources with the vortex pairing locations. Laufer & Yen (1983) also found that the acoustic field of a forced round jet was consistent with stationary sources, and associated the sources with the nonlinear saturation of the unstable wave amplitudes at the vortex pairing locations. Huerre & Crighton (1983) showed that the results of Laufer & Yen were inconsistent with certain features of Lighthill's (1952) theory. Later they showed that the inconsistency could be resolved by analysing the superdirective nature of the acoustic sources (Crighton & Huerre 1990). Mankbadi (1990) used Laufer & Yen's curve fits for the growth and decay of instability waves to determine the acoustic source term for Lighthill's equation. He showed that a superdirective acoustic field results. It is worth noting that Bridges & Hussain (1992) also measured an acoustic field (of a forced jet) consistent with stationary sources, though they did not find a superdirective acoustic field.

1.1. *Overview of the present investigation*

The remainder of this section is devoted to a brief review of previous theoretical results relevant to the present study. Aeroacoustic theory is discussed in general in §1.2 and Lilley's equation in particular in §1.3.

In §2, the results of the DNS of the mixing layer are presented. For brevity, many details regarding the numerical method are omitted – details of the scheme are presented in Colonius, Lele & Moin (1995). In order to investigate the sound generated by vortex roll up and pairings without the additional complication of 'random' fine-grained turbulent fluctuations the mixing layer is forced at its most unstable frequency, f, and the first three subharmonics, $f/2$, $f/4$ and $f/8$, respectively. The resulting flow field is highly organized and nearly periodic in time. The two vortex pairing locations are fixed in space and the generated acoustic field is dominated by waves at the frequencies of the vortex pairings. The acoustic field at other frequencies is very much smaller. The computational domain is not long enough to capture a third pairing of the vortices.

In §3, Lilley's acoustic analogy is considered. It is shown that the acoustic field from the DNS is in excellent agreement with the acoustic analogy prediction. However, the predicted acoustic field is extremely sensitive to the details of how the source terms are computed. The computational details of the sensitivity are particular to the methodology used here and may be of limited interest to the general reader. Thus they are discussed in the Appendix.

The remainder of §3 is devoted to the details of the acoustic sources and the far-field directivity produced by the vortex pairings. In §3.3 the full ('exact') acoustic source is analysed and compared to the simplified quadrupole source proposed by Goldstein (1976*a*, 1984). The predicted acoustic field is inconsistent with certain rationales which have in the past been put forth for the neglect of certain parts of the full acoustic source. An alternative explanation for the efficacy of Goldstein's quadrupole source term is put forward by exploiting a connection between the acoustic analogy and an asymptotic expansion of the flow. In §3.4, the radiation of compact quadrupole

sources in the present layer is considered and it is shown there that the source structure and directivity of the present flow are not well modelled by compact quadrupoles. In §3.5 it is shown that a relatively simple 'superdirective' radiation model (Crighton & Huerre 1990) is in reasonable agreement with the computational results. Finally, flow–acoustic interactions are discussed in §3.6.

1.2. *Aeroacoustic theory*

The prediction of the sound which is generated by turbulent flows has been extensively researched since Lighthill (1952, 1954) first proposed the acoustic analogy for turbulent jets. In his acoustic analogy, the jet flow is replaced by a distribution of acoustic sources (stationary or convecting) in an ambient fluid at rest. Lighthill's equation is 'exact' (it is a rearrangement of the Navier–Stokes and continuity equations) but it is a single equation in several dependent variables, and only yields predictions if the source terms are known *a priori*. Detailed experimental measurements of the source term (and its retarded time) would be very difficult and have never been performed. Thus, simplifying assumptions about the forms of the source terms have been used to predict scaling laws and the directivity of the acoustic field. In certain cases the theory and its subsequent modifications is in good agreement with experiments, but it can be argued that no theory yet satisfactorily predicts subsonic jet noise without a good deal of empirical input (Tam 1995).

Crow (1970) examined the theory of aerodynamic sound generation with singular perturbation methods and showed that Lighthill's equation is equivalent to a matched asymptotic expansion of a low-Mach-number flow when the length scale of an eddy *and* the extent of the vortical flow surrounding that eddy are both small compared to the acoustic wavelength. The mathematical difficulty stems in part from the inability of the acoustic analogy to extract the sound 'generation' problem from the interaction of acoustic waves with turbulence and the mean flow. The flow considered here has an extensive vorticity field which leads to significant flow–acoustic interaction. It is possible to overcome some of these difficulties by moving certain terms from Lighthill's source term to the left-hand side of the equation, as was done by (amongst others) Lilley (1974) and described by Doak (1972), and Goldstein (1976*a*, 1984). An unambiguous description of the sources can be obtained by carrying out, to second order, a systematic asymptotic expansion which treats the unsteady flow as a small perturbation to a parallel mean flow (Goldstein 1984). However, such linear expansions are at best only locally valid, and ultimately nonlinear effects will dominate the near-field disturbances and cause the expansion to break down. Since the acoustic far field depends on a global solution to the problem, this approach does not lead to a rigorous first-principles method for calculating the sound field (Goldstein 1984). In that case one must again regard the source term as independently known (as in Lighthill's acoustic analogy).

Thus, to date no acoustic analogy theory has been successful in fully isolating the source terms from terms which are linear in the acoustic perturbations for a spreading shear flow. However, from a computational point of view, it is possible, within the accuracy limits of the computation, to evaluate any particular 'exact' source term of an acoustic analogy (whether or not it includes such linear flow–acoustic interaction terms) and predict the radiated acoustic field. Such results are presented here for Lilley's acoustic analogy. The reasons for concentrating on Lilley's equation are twofold. First, Lilley's equation (in its form discussed in §1.3) allows for a mean flow which incorporates the unequal convection velocities on either side of the mixing layer, and some approximation of the mean shear through the layer. Though Lighthill's

second-order equation may be written so that the left-hand side is the convective wave operator in a uniform flow (the equations of motion are Galilean invariant), the unequal convection velocities above and below the mixing region require that two different equations be written for each side of the layer and that their solution be matched at the centre. This was in fact done by Ffowcs Williams (1974) and Dowling, Ffowcs Williams & Goldstein (1978), where the acoustic field arising from convecting sources in a mixing layer was computed in the vortex sheet limit. However, the acoustic sources computed from the DNS data depend on the mean flow shear and its spreading and vary smoothly across the layer. As shown *a posteriori* in §3.6, flow–acoustic interaction is significant in the mixing layer (despite the relatively low Mach number considered here), and the prediction for the radiated acoustic field is sensitive to the particular form of the velocity profile used in the wave propagation operator (left-hand side) of Lilley's acoustic analogy (see equation (2), below).

1.3. *Lilley's equation*

Lilley's (1974) third-order wave equation can be obtained by combining the equations describing conservation of mass and momentum in a compressible fluid:

$$\frac{\mathrm{D}}{\mathrm{D}t}\left(\frac{\mathrm{D}^2\Pi}{\mathrm{D}t^2}-\frac{\partial}{\partial x_j}\left(a^2\frac{\partial \Pi}{\partial x_j}\right)\right)+2\frac{\partial u_k}{\partial x_j}\frac{\partial}{\partial x_k}\left(a^2\frac{\partial \Pi}{\partial x_j}\right)=-2\frac{\partial u_j}{\partial x_k}\frac{\partial u_i}{\partial x_j}\frac{\partial u_k}{\partial x_i}, \qquad (1)$$

where $\Pi = (1/\gamma)\ln p$. Equation (1) is an exact equation except for the viscous terms which have been omitted – they are generally thought to contribute very little to the acoustic field (e.g. Goldstein 1976*a*). In equation (1) and in what follows p is the pressure normalized with $\rho_\infty a_\infty^2$, where ρ_∞ and a_∞ are the density and sound speed far from the mixing region and are equal in both streams; u_i are the Cartesian components of the velocities normalized by a_∞; x_i are the spatial coordinates normalized with δ, the vorticity thickness of the layer at $x_1 = 0$ (defined in §2.1.2); and t is time is normalized by δ/a_∞. The fluid is assumed to be an ideal gas so that $a^2 = \gamma p/\rho$, where γ is the (assumed constant) ratio of specific heats.

Unlike Lighthill's equation, the left-hand side of Lilley's equation is nonlinear. The usual approach (see, for example, Goldstein 1976*a*), is to linearize it about a time-independent base flow. Below, such a linearization of the left-hand-side is performed, but all terms removed from the left-hand side are taken to the right-hand side, i.e. added to the source term. Thus the equation will still be exact. Because the mean of a turbulent shear layer varies much more slowly with x_1, the streamwise coordinate, than with x_2, the coordinate normal to the layer, the time-independent base flow is often taken to be a parallel flow with a streamwise velocity, $U(x_2)$ (giving $u_1(x_1, x_2, t) = U(x_2) + u_1'(x_1, x_2, t)$), and zero normal velocity ($u_2(x_1, x_2, t) = u_2'(x_1, x_2, t)$). The pressure and speed of sound are taken to be uniform (Goldstein 1976*a*) and thus for an ideal gas $\Pi(x_1, x_2, t) = (1/\gamma)\ln(1/\gamma) + \Pi'(x_1, x_2, t)$, and $a^2(x_1, x_2, t) = 1 + a^{2'}(x_1, x_2, t)$. Note that $a^{2'}$, the departure of the speed of sound from its value in the base flow, is equivalent to departures from the base flow temperature, since the fluid is considered to be a perfect gas. Then the parallel flow velocity, $U(x_2)$, is chosen to correspond with the true mean streamwise velocity of the mixing layer at a particular value of x_1. Unless otherwise noted the mean streamwise velocity of the DNS at $x_1 = 0$ is used for $U(x_2)$. The effect of making a different choice is discussed below in §3.6.

The resulting equation is

$$\frac{\mathrm{D}_o}{\mathrm{D}t}\left(\frac{\mathrm{D}_o{}^2\Pi'}{\mathrm{D}t^2}-\frac{\partial}{\partial x_j}\left(\frac{\partial\Pi'}{\partial x_j}\right)\right)+2\frac{\partial U}{\partial x_2}\frac{\partial^2\Pi'}{\partial x_1\partial x_2}=\Gamma, \tag{2}$$

where $\mathrm{D}_o/\mathrm{D}t=\partial/\partial t+U(x_2)\partial/\partial x_1$, and Γ is given by

$$\begin{aligned}\Gamma \;=\; & \frac{\mathrm{D}_o}{\mathrm{D}t}\Bigg(\underbrace{\frac{\partial^2 u_i'u_j'}{\partial x_i x_j}}_{\text{Term Ia}}-\underbrace{\frac{\partial u_i'}{\partial x_i}\frac{\partial u_k'}{\partial x_k}}_{\text{Term IIa}}+\underbrace{\frac{\partial}{\partial x_j}\left(a^{2\prime}\frac{\partial\Pi'}{\partial x_j}\right)}_{\text{Term IIIa}}+\underbrace{a^2\frac{\partial\Pi'}{\partial x_i}\frac{\partial\Pi'}{\partial x_i}}_{\text{Term IVa}}\\ & \underbrace{+\frac{\partial\Pi'}{\partial x_j}\left(u_i'\frac{\partial u_j'}{\partial x_i}\right)+u_j'\frac{\partial}{\partial x_j}\left(u_i'\frac{\partial\Pi'}{\partial x_i}\right)}_{\text{Term Va}}\Bigg)\\ & -2\frac{\mathrm{d}U}{\mathrm{d}x_2}\Bigg(\underbrace{\frac{\partial^2 u_2'u_j'}{\partial x_1 x_j}}_{\text{Term Ib}}-\underbrace{\frac{\partial u_2'}{\partial x_1}\frac{\partial u_k'}{\partial x_k}}_{\text{Term IIb}}+\underbrace{\frac{\partial}{\partial x_1}\left(a^{2\prime}\frac{\partial\Pi'}{\partial x_2}\right)}_{\text{Term IIIb}}+\underbrace{a^2\frac{\partial\Pi'}{\partial x_1}\frac{\partial\Pi'}{\partial x_2}}_{\text{Term IVb}}\\ & \underbrace{+\frac{\partial\Pi'}{\partial x_1}\left(u_2'\frac{\partial u_i'}{\partial x_i}\right)+u_i'\frac{\partial}{\partial x_1}\left(u_2'\frac{\partial\Pi'}{\partial x_i}\right)}_{\text{Term Vb}}\Bigg).\end{aligned} \tag{3}$$

Equation (2) with the source given by equation (3) remains exact regardless of the time-independent parallel base flow chosen. Note that the nonlinear Euler equations (written in terms of the base flow and primed quantities) have been used in writing the source in the form of equation (3). For ease of future reference, the various parts of the source have been labelled with Roman numerals. Each term has two parts, part (a) which is convected with the parallel base flow, and part (b) which is sheared by the parallel base flow. In what follows, when we refer to a Roman numeral alone (without the suffix a or b), we mean both parts taken together.

The form in which the source term, equation (3), has been written is motivated by Goldstein's (1976*a*, 1984) analysis, where a simplified version of the source is proposed:

$$\Gamma\approx\frac{\mathrm{D}_o}{\mathrm{D}t}\Bigg(\underbrace{\frac{\partial^2 u_i'u_j'}{\partial x_i x_j}}_{\text{Term Ia}}\Bigg)-2\frac{\mathrm{d}U}{\mathrm{d}x_2}\underbrace{\frac{\partial^2 u_2'u_j'}{\partial x_1 x_j}}_{\text{Term Ib}}. \tag{4}$$

Note that equation (4) was derived in two different ways in Goldstein (1976*a*) and Goldstein (1984). The details of the different derivations are of importance, and are discussed below in §3.3. Equation (4) is of an appealing form because it extends Lighthill's (1952) concept of a quadrupole source distribution to parallel shear flows (Goldstein 1976*a*, 1984). That is, the source given by equation (4) is equivalent to that which would be produced by an external distribution of stresses, $u_i'u_j'$, imposed on a parallel shear flow.

2. Direct numerical simulations

2.1. *Methodology*

2.1.1. *Approach and computational issues*

As is discussed by Lighthill (1992), computations of aerodynamic sound generation can be broadly divided into three strategies. (i) The computational domain includes only the near-field region without attempting to resolve the acoustic waves. Subsequently an acoustic analogy is solved with source terms that have been determined from the near-field computations. (ii) The computational domain includes the near-field region and, to a small extent, the acoustic region. The acoustic far field is deduced by solving the wave equation in the exterior domain given boundary data from the near field. (iii) The computational domain includes both the near field and a significant portion of the acoustic field. Both regions are solved using the compressible Navier–Stokes equations.

For subsonic flows, category (iii) computations are difficult for several reasons (Crighton 1986, 1993): the large extent of the acoustic field compared to the flow field; the very small energy of the acoustic field relative to the flow field; and the possibility that numerical discretization itself may act as a more significant source of sound than the continuous flow field which is approximated. A fourth difficulty is the application of accurate free-space boundary conditions appropriate at an artificial computational boundary. The latter three difficulties are also encountered in category (ii) computations. Computations in category (ii) rely on the so-called Kirchhoff surface surrounding the acoustic sources to predict the far field. The linear Kirchhoff surface theory inevitably breaks down at regions where flow structures leave the computational domain and linear equations do not hold; such issues are at present being investigated (e.g Lyrintzis 1993; Freund, Lele & Moin 1995; Mitchell, Lele & Moin 1996). By contrast, category (i) computations do not rely on resolving the acoustics and can be performed with existing incompressible DNS codes. For this reason, Lighthill (1992) at present urges using strategy (i) for low Mach number flows. This approach is not without its own difficulties. In particular, it is difficult to evaluate the integrals in the acoustic analogies accurately (e.g. Sarkar & Hussaini 1993).

Computational aeroacoustics is a relatively new field and time will tell which methods yield the best results. It may be that all three categories are useful for their own subset of problems. At present, investigations in categories (ii) and (iii), we would argue, promise to yield more fundamental knowledge about the sound generation process, since they allow an exploration of flow problems for which the use of the acoustic analogy approach requires assumptions whose validity is not know *a priori* .

In the present study, the computational resources required to compute both the near and far fields together is large and therefore only a two-dimensional flow has been computed. This allows a relatively large portion of the acoustic field to be computed and flow features are very well resolved. Even for the two-dimensional mixing layer considered here several hundred CPU hours on the CRAY Y-MP supercomputer were required. To accurately resolve the compressible flow and its generated acoustic field, fourth- and sixth-order-accurate compact finite difference schemes (Lele 1992) and fourth-order Runge–Kutta time marching are used. These schemes have very small inherent dissipation and give a highly accurate representation of wave propagation. Non-reflecting boundary conditions (see the review by Givoli 1991) are used at all computational boundaries. Giles (1990) provided approximate

non-reflecting boundary conditions for the linearized Euler equations. While such linear boundary conditions are sufficiently accurate for acoustic waves exiting the computational domain at various angles (such as the inflow and normal boundaries of the present problem), the accuracy of the boundary conditions at the outflow boundary where large-scale non-acoustic flow structures (i.e. fluctuations whose magnitude is a considerable percentage of the mean flow) is poor (Colonius, Lele & Moin 1993). To circumvent this problem, we use a technique where, in a region of the computation just upstream of the outflow, a combination of grid stretching (in the streamwise direction) and low-pass filtering (applied spatially) effectively reduce the amplitudes of fluctuations before they interact with the downstream boundary, thus diminishing the reflections. Previous experiments with the 'sponge region' showed that spurious reflections were reduced in amplitude by as many as 3 orders of magnitude over the linearized boundary conditions alone (Colonius *et al.* 1993). The sponge region does have some impact on the computation of the acoustic sources, but it was found that the damping of the sources provided by the sponge was not a significant source of sound in the computations (Colonius *et al.* 1995).

The present numerical scheme has been validated by solving a number of model problems including the interaction of sound waves with a two-dimensional vortex (Colonius, Lele & Moin 1994), and the sound produced by a pair of co-rotating vortices (Mitchell, Lele & Moin 1995). These computations gave good agreement with both experimental and theoretical predictions. Finally a similar method has recently been applied to a axisymmetric jet flow by Mitchell *et al.* (1996).

2.1.2. *Flow and computational configuration*

The two-dimensional, unsteady, compressible Navier–Stokes equations plus continuity, conservation of energy, and the perfect gas equation of state are solved numerically. Independent and dependent variables are non-dimensionalized as discussed in §1.3. In particular, lengths are made non-dimensional with the vorticity thickness of the layer at $x_1 = 0$:

$$\delta = \left(\frac{\Delta U}{|\partial u_1 / \partial x_2|_{max}} \right)_{x=0}, \tag{5}$$

where ΔU is the difference in velocity across the layer.

The Mach numbers of the high- and low-speed streams are $M_1 = 0.5$ and $M_2 = 0.25$, respectively. The Reynolds number, based on the vorticity thickness and velocity difference across the layer, $Re = \rho_\infty \Delta U \delta / \mu$ is 250. The temperatures of the two free streams are equal. Given the relatively low Mach numbers and equality of temperature in the free streams, temperature dependence of the transport properties is not likely to be a significant effect. Therefore the molecular viscosity, μ, and thermal conductivity, k, are taken to be constant, and $Pr = c_p \mu / k = 1$. The ratio of specific heats, γ, is taken to be 1.4.

The initial condition for the mixing layer is the laminar solution to the steady compressible two-dimensional boundary layer equations. The boundary layer equations and solution method are given by Sandham & Reynolds (1989). The dividing streamline of the layer is chosen to fall below $x_2 = 0$ such that initially the normal velocity is directed into the computational domain at the normal boundaries, as is the case later after the layer rolls up into vortices and pairs. Thus at the normal boundaries inflow boundary conditions hold for all time.

The computational domain extends to $x_2 = \pm 200$ and $x_1 = 285$, not including the sponge region (recall that lengths are made dimensionless with the vorticity thickness,

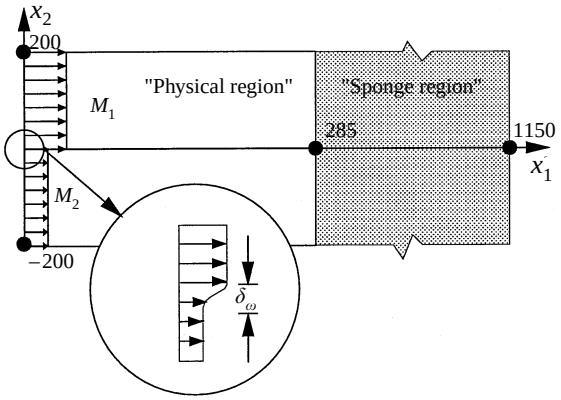

FIGURE 1. Schematic diagram of computational domain.

δ). The sponge region extends from $x_1 = 285$ to $x_1 = 1150$. A schematic diagram of the flow including the initial laminar velocity profile at $x_1 = 0$ is shown in figure 1. A Cartesian grid of 2300 by 847 grid points in the x_1- and x_2-directions, respectively, is used. The grid in x_1 is uniform with spacing $\Delta x_1 = 0.15$ up to $x_1 = 285$. In the sponge the grid is highly stretched over the last 400 nodes. The grid is stretched in the normal direction such that it is very nearly uniform with a fine grid spacing of $\Delta x_2 = 0.15$ in a region around $x_2 = 0$, and nearly uniform, but with a coarser spacing of $\Delta x_2 = 0.80$ for large $\pm x_2$. Smooth functions are used for the mesh stretching in both directions (Colonius *et al.* 1995). The time step, Δt, was 0.0567, chosen to give an integral number of time steps in the period of the fundamental frequency of the layer. The maximum CFL number of the computation is roughly 3 times smaller than the stability limit of the current scheme ($CFL < 1.43$, Colonius *et al.* 1995). Grid resolution studies on the near-field portion of the layer were performed, and it was found that a computation with double the grid spacing in the x_1-direction (i.e. $\Delta x_1 = 0.30$), and roughly 1.5 times the grid spacing in x_2 gave very nearly identical results for the near-field portion of the present grid. Note that the high spatial and temporal resolution were chosen to ensure that the flow variables were sufficiently well resolved to allow the repeated differentiations of the data necessary to compute the source terms to be performed accurately.

2.1.3. *Eigenfunction forcing*

The flow is forced at the inflow ($x_1 = 0$) with eigenfunctions (linearized disturbances) found by solving Rayleigh's equations for a velocity profile corresponding to the viscous mean flow at $x_1 = 0$. The eigenfunctions are determined by the method given by Sandham & Reynolds (1989). The two-dimensional spatially growing disturbances have the form:

$$g'(x_1, x_2, t) = \tilde{g}(x_2)\mathrm{e}^{2\pi\mathrm{i}(\alpha x_1 - \omega t)}, \tag{6}$$

where g is any of u_1, u_2, ρ or p, and where the tilde denotes the complex eigenfunctions. Here $\alpha = \alpha_R + \mathrm{i}\alpha_I$ is the complex wavenumber in the x_1-direction, normalized by the inverse of the vorticity thickness defined by equation (5), and ω is the real frequency, normalized by the speed of sound divided by the vorticity thickness. The factor of 2π in the exponential term in equation (6) gives α and ω in units of the *circular* wavenumber and frequency respectively. The eigenfunctions for each frequency are normalized with respect to the maximum value of $|\tilde{u}_1(x_2)|$, and then multiplied by a

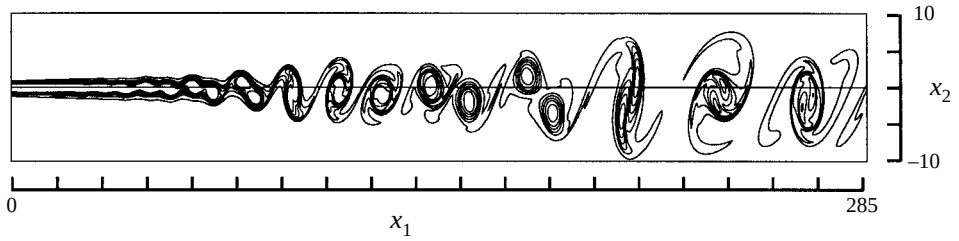

FIGURE 2. Vorticity contours in near-field mixing region. The normal axis is expanded by a factor of 2.5. Contour levels: min: −0.13, max: 0.01, increment: 0.02.

small amplitude ratio. The amplitude ratio is chosen such that the maximum value of $|\tilde{u}_1|$ is 0.001 times the velocity of the high-speed stream. The eigenfunctions are then added together, with the phase of the first three subharmonics (relative to the fundamental) being adjusted such as to minimize the distance between pairings. The fundamental frequency, $\omega = f$, for the current mixing layer is 0.0501, and the wavenumbers, α, are $(0.131 - 0.0193\mathrm{i})$, $(0.0635 - 0.0146\mathrm{i})$, $(0.0309 - 0.00852\mathrm{i})$, and $(0.0152 - 0.00454\mathrm{i})$ for frequencies f, $f/2$, $f/4$ and $f/8$ respectively. The phase shifts of the subharmonics (in radians relative to the phase of the fundamental) are: −0.028, 0.141, and 0.391 for $f/2$, $f/4$ and $f/8$, respectively.

Note that the specification of the forcing at the inflow must be done in a way which is compatible with the non-reflecting boundary conditions used at the inflow. The incoming instability waves are added to the the incoming (one-dimensional) characteristics (the form of which, relative to the mean flow at $x_1 = 0$, is given by Colonius *et al.* 1993). Done in this way, the forcing does not affect the accuracy of the non-reflecting boundary condition for the upstream propagating acoustic wave. Since the non-reflecting boundary conditions are not exact (they are an approximation valid for waves propagating at angles close to normal to the boundary), some error (i.e. incoming acoustic wave) is generated by the forcing. This error is discussed in §§ 2.3 and 3.2.

2.2. *Evolution of the near-field region*

The instantaneous vorticity at a time corresponding to 68 periods of the fundamental frequency is shown in figure 2. The vorticity contours plainly show the roll-up and two subsequent pairings. Figure 3 shows time traces of the streamwise velocity at $x_2 = 0$ for various streamwise locations downstream of the inflow boundary. At the first location, $x_1 = 0$ (inflow), the forcing is felt instantly, and all components of the forcing are felt equally. The start-up transient is seen to arrive at points downstream at progressively later times. The growth and relative dominance of the different forcing frequencies can be seen at points further downstream. Evidently the layer becomes nearly periodic in time over the entire length of the physical domain after about $48T$.

The frequency content of the mixing layer can be found by taking a discrete Fourier transform (DFT) of the nearly periodic data. Errors in the value of the transform at a particular frequency can arise if the signal $F(t_j)$ is not sampled sufficiently fast or if the total duration of the signal is not sufficiently long. It was found (Colonius *et al.* 1995) that by sampling the DNS data at a rate of $22\Delta t$ (corresponding to 16 samples per fundamental period, T) aliasing effects (both in the transforms of the primitive variables and in products and differentiations of products which arise in the acoustic source terms) are negligible at frequencies up to $2f$, which is at the high end of frequencies relevant to the present study. A total time of $112T$ was computed,

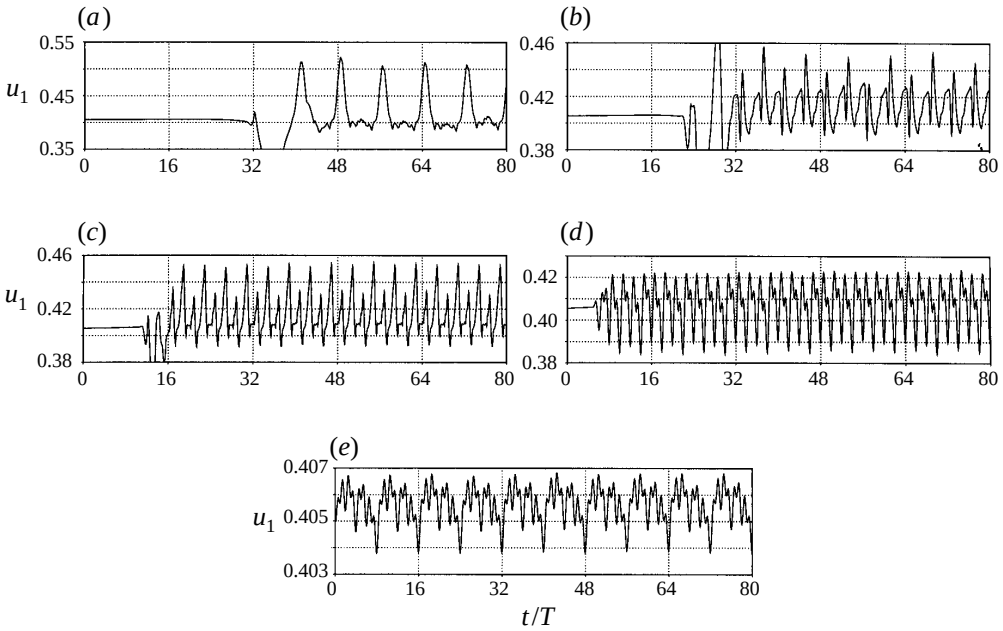

FIGURE 3. Streamwise velocity, u_1, as a function of time (normalized by the period of the fundamental frequency, $T = 1/f$) at $x_2 = 0$ and various streamwise locations. (*a*) $x_1 = 285.0$, (*b*) $x_1 = 200.0$, (*c*) $x_1 = 100.0$, (*d*) $x_1 = 45.0$, (*e*) $x_1 = 0$.

of which the last $64T$ is after the entire domain has settled into its nearly periodic steady state. Thus 8 periods of the lowest forced frequency, $f/8$, are available for the DFT. Since the data are not strictly periodic, windowing and data segmenting (e.g. Press *et al.* 1989) can be used to increase the accuracy of the power spectrum in a particular frequency bin. Such techniques were evaluated (Colonius *et al.* 1995), and it was found that the spectra of the primary dependent variables (e.g. u_1, u_2, etc.) are not very sensitive to the details of the DFT. Differing techniques, data lengths, etc. led to at most a 5% difference in the amplitude of the spectra throughout the layer. Note that the same is true for the measured acoustic waves and sources, but not for the acoustic analogy predictions, which turn out to be extremely sensitive to small differences in the values of the DFT as discussed in the appendix.

The growth, saturation and decay of the different modes can be seen by plotting the energy, $E(\omega)$, as a function of x_1 for $\omega = f$, $f/2$, and $f/4$. $E(\omega_n)$ is defined by

$$E(\omega) = \int_{-L}^{+L} |\hat{u}_{1\omega}|^2 \mathrm{d}x_2 \tag{7}$$

where $\pm L$ is the upper and lower extent of the computational domain. For each of the fundamental and first two subharmonics an exponential growth of the energy is followed by saturation and eventual decay. The saturation of the fundamental frequency, f, and its subharmonics $f/2$ and $f/4$ occurs near $x_1 = 50$, 75, and 175, respectively.

2.3. *Evolution of the far-field region*

Away from the mixing region fluctuations become very small and nonlinear effects are negligible. In this region the mean flow is nearly uniform with a single component M_1

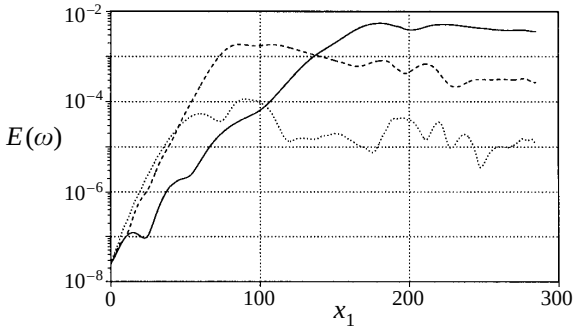

FIGURE 4. Energy, $E(\omega)$, as a function of x_1: ·····, $\omega = f$; - - - -, $\omega = f/2$; ——, $\omega = f/4$.

(for $x_2 > 0$) or M_2 (for $x_2 < 0$). There is a small mean value of the normal velocity directed into the computational domain at both the top and bottom boundaries because the layer entrains fluid due to the mean flow spreading.

Small fluctuations in the far field are discrete Fourier transformed into frequency space as discussed in the last section. Results are given here for the dilatation, $\Theta = \partial u_i/\partial x_i$, in the far field. The dilatation is chosen to best display the acoustic waves in the far field. The pressure shows very similar fluctuations, but is slightly contaminated by a very slow drift in its value with time. The pressure drift, which arises because of the non-reflecting boundary conditions, is not a serious problem in the computation – the change in pressure over $64T$ is just 0.03% of its ambient value (Colonius *et al.* 1995). The dilatation is directly related to the acoustic pressure. In the high-speed stream, at large x_2,

$$\frac{\partial p'}{\partial t} + M_1 \frac{\partial p'}{\partial x_1} = -\Theta. \tag{8}$$

For the low-speed stream at large $-x_2$, M_1 is replaced by M_2 in equation (8). Since the dilatation is related to the time derivative of the pressure and the drift in the pressure signal is nearly linear, the drift shows up as a small mean value added to the dilatation. The dilatation is therefore more nearly periodic in time than the pressure and thus the DFT can be computed with less contamination of the low and high frequencies.

In figure 5, contours of the real part of the DFT of the dilatation are plotted away from the sheared region at four different frequencies: the fundamental, f, its first two subharmonics, $f/2$ and $f/4$, and an unforced frequency $3f/2$. Note that the real part of the DFT corresponds to a particular (but arbitrarily chosen) phase. The saturation locations for the instability waves are indicated on the plots along the x_1-axis. It is evident that the acoustic waves at the first two subharmonic frequencies emanate from the region of the layer where the instability waves at those frequencies saturate. That is, the acoustic waves at the subharmonics appear to emanate from the regions where the pairings occur. This is similar to the observations of Laufer & Yen (1983) and Bridges & Hussain (1992), and to the analysis of Mankbadi & Liu (1984), Crighton & Huerre (1990), and Mankbadi (1990). It appears also that the waves are primarily focused downstream, reaching their maximum amplitude (for a given distance from their apparent origin) near the $+x_1$-axis.

The computations of the acoustic field at the fundamental frequency, f, have maximum amplitude in directions nearly normal to the layer (at least for the portion of the field downstream of the inflow boundary). The waves also appear to emanate

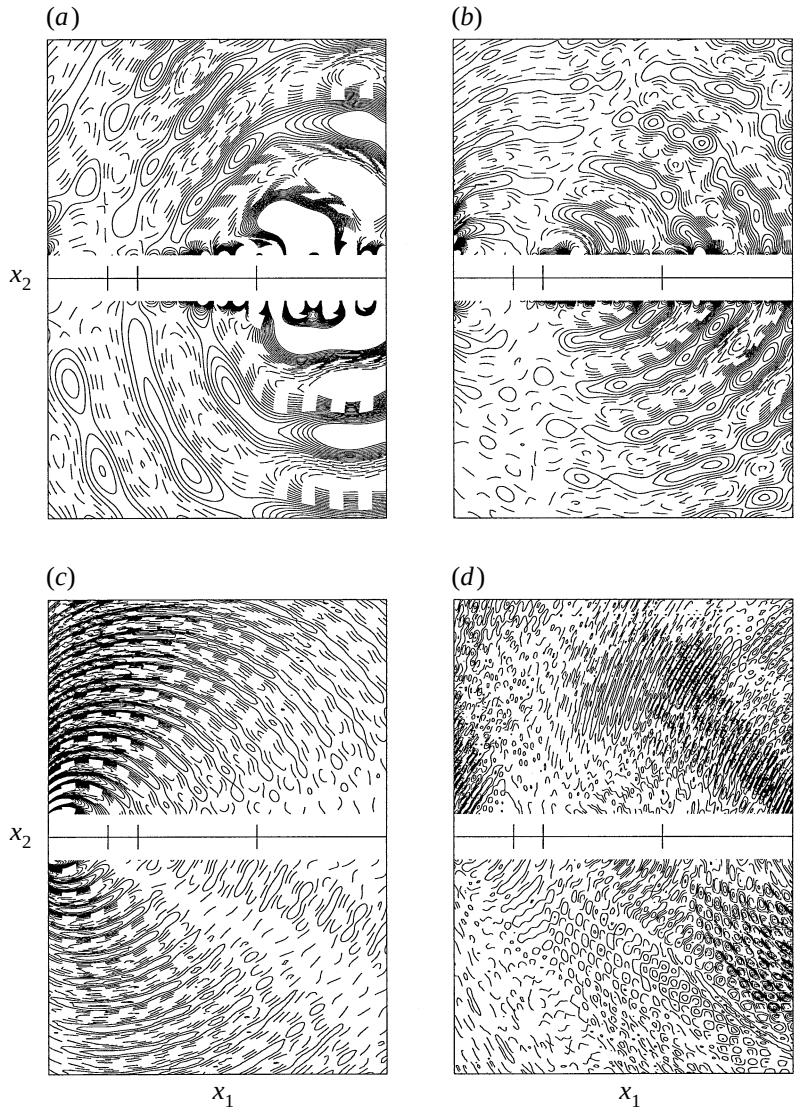

FIGURE 5. Contours of the real part of the DFT of the dilatation away from the sheared region for several frequencies: (*a*) $f/4$, (*b*) $f/2$, (*c*) f, (*d*) $3f/2$. The entire domain (except sponge) is shown. The approximate saturation locations for the fundamental frequency and its first two subharmonics are indicated on the plot with the tic marks on the x_1-axis at $x_1 = 50$, 75 and 175, respectively. Dashed lines are negative contours and solid lines are zero and positive contours. Contour levels (all times 10^6): (*a*) -1.0 to 1.0 at intervals of 0.1; (*b*) -0.4 to 0.4 at intervals of 0.04; (*c*) -0.2 to 0.2 at intervals of 0.02; (*d*) -0.004 to 0.004 at intervals of 0.0004.

from a region upstream of the saturation location for the fundamental frequency, at a location very near the inflow boundary. These waves are an artifact of the instability wave forcing at the inlet (Colonius *et al.* 1995). Approximations in the non-reflecting boundary conditions used at the inflow make it impossible to entirely eliminate any spurious incoming wave from the inlet forcing. The amplitude of the acoustic waves shown in figure 5(*c*) is roughly 5000 times smaller than the amplitude of the inlet forcing, indicating that the error is very small indeed. It appears that any sound at the

fundamental frequency which is actually generated by the flow is at a smaller level. Upon further examination of the dilatation fields at the subharmonic frequencies, it appears that some contamination from the inlet forcing is also present – waves can be seen emanating from a region very near the inflow. These waves appear to have their highest amplitude along the inlet boundary. They are of comparable magnitude to those emanating near the inflow at the fundamental frequency – however they are, in the case of the subharmonics, smaller than those waves which are produced by the flow itself.

For the unforced frequency, $3f/2$, spurious acoustic waves emanating from the outflow boundary (sponge region) are evident. In fact, such spurious waves are found for nearly all the frequencies except those explicitly forced (the results for additional frequencies can be found in Colonius *et al.* 1994*b*). Some waves produced near the region of the first pairing are also evident, but the field is seriously contaminated by the waves produced downstream of the physical domain. The amplitude of these spurious waves, at both $3f/2$ and all other unforced frequencies, is at least an order of magnitude smaller than the waves at the forced frequencies. Evidently the sound generated by the flow within the physical part of the domain is also very much smaller for the unforced frequencies. Note that spurious reflections from the sponge at the *forced* frequencies, if they exist, are of sufficiently small amplitude so as to be undetectable compared to the actual sound generated within the physical computational domain. The presence of these spurious waves indicates the need for further refinements to the downstream boundary conditions.

3. Acoustic analogy solution

3.1. *Numerical solution of Lilley's equation*

Unlike the standard wave equation, an exact Green's function for equation (2) is not known. However, since the acoustic analogy is to be solved for a source term which is only known numerically (that is from DNS on a finite number of computational nodes), the acoustic analogy must also be solved numerically. Since the non-constant coefficients in equation (2) depend only on the normal coordinate, x_2, the equation can be reduced to an ODE by performing a Fourier transform in x_1 and t and there is little additional complication or expense to solving Lilley's equation compared to acoustic analogies for which exact Green's functions exist.

Because the Fourier transform in time is used, only the sound that is produced after a periodic state has been reached is considered. It is assumed that the source term decays sufficiently rapidly downstream so that its Fourier transform (in x_1) is well defined and that the sources are not significantly altered by the presence of the sponge region. These last two assumptions have been verified in detail (Colonius *et al.* 1995).

Equation (2) is discretized over a finite period of time, T, such that $t_j = Tj/N$ with $j = 0, 1, \cdots, N-1$, where N is the number of samples. The variable x_1 is left in continuous form, and thus the transformed pressure perturbation is defined by

$$\hat{\Pi}_n(k, y) = \frac{1}{N} \sum_{j=0}^{N-1} \int_{-\infty}^{+\infty} \Pi'(x_1, x_2, t_j) \mathrm{e}^{-2\pi \mathrm{i}(kx_1 + jn/N)} \mathrm{d}x_1. \tag{9}$$

Now let

$$\phi_n(k, x_2) = (\omega_n + Uk)^{-1} \hat{\Pi}_n(k, x_2). \tag{10}$$

Transforming equation (2) according to equations (9) and (10) gives

$$\phi_n'' + \lambda_n^2(k, x_2)\phi_n = \frac{-G_n(k, x_2)}{2\pi \mathrm{i}(\omega_n + Uk)^2}, \tag{11}$$

where the prime denotes differentiation with respect to x_2, G_n is the Fourier transform of the source term, Γ, and

$$\lambda_n^2 = \left[4\pi^2\left((\omega_n + Uk)^2 - k^2\right)\right] + \left[-(\omega_n + Uk)((\omega_n + Uk)^{-1})''\right], \tag{12}$$

where $\omega_n = n/T$.

When $\lambda^2 > 0$ the solutions to equation (11) are oscillatory; for $\lambda^2 < 0$ the solutions are damped exponentially for large $|x_2|$. λ^2 is positive, for large x_2, on at least one side of the layer when:

$$\frac{-\omega_n}{1 + M_2} < k < \frac{\omega_n}{1 - M_1}. \tag{13}$$

Boundary conditions depend on the sign of λ_n^2 as $x_2 \to \pm\infty$. For $\lambda_n^2 < 0$, the correct boundary condition is that ϕ_n decays. For $\lambda_n^2 > 0$, the Sommerfeld radiation condition (in one dimension) should be applied:

$$\phi_n' + \mathrm{i}(\lambda_n^2)^{1/2}\phi_n = 0, \qquad x_2 \to +\infty, \tag{14a}$$

$$\phi_n' - \mathrm{i}(\lambda_n^2)^{1/2}\phi_n = 0, \qquad x_2 \to -\infty, \tag{14b}$$

where the positive branch of the square-root function is used for ω_n positive and the negative branch is used for ω_n negative.

Note that equation (2) also admits causal solutions, for a particular frequency, which grow exponentially in x_1 (i.e. the instability waves of the layer, see Dowling *et al.* 1978). When the phase speed of these waves is subsonic they decay exponentially fast on either side of the layer (Tam & Morris 1980). Thus in solving equation (2) we ignore the unbounded solutions (note that the instability waves have phase speeds which fall outside the bounds of the integration in equation (15)), since they have negligible impact on the acoustic farfield.

A numerical method for solving equation (11) is discussed by Colonius *et al.* (1994*b*). The infinite domain in x_2 is mapped to a finite computational region and finite differences are used for the derivatives. An important aspect of the scheme is that the oscillatory nature of the solutions to equation (11) for large $|x_2|$ is accounted for analytically by a change of dependent variable. The code has been validated with grid resolution studies, and by comparison with a solution to the full Euler equations for a specified source term as described by Colonius *et al.* (1995). Solving equation (11) requires the source term Γ to be discrete Fourier transformed in t and continuously Fourier transformed in x_1. Numerical quadrature is used to compute the continuous Fourier transform. Since the transform need only be performed for values of k given by equation (13) and we are interested in the low frequencies, the exponential factors in the quadrature do not oscillate too rapidly to obtain an accurate solution. The details of the integration and its validation are discussed by Colonius *et al.* (1995). The effect of the attenuation of the acoustic sources in the sponge outflow region was also investigated by Colonius *et al.* (1995) and found to not significantly impact the predicted acoustic fields.

Once the solution to equation (11) is found, the pressure and dilatation (at discrete

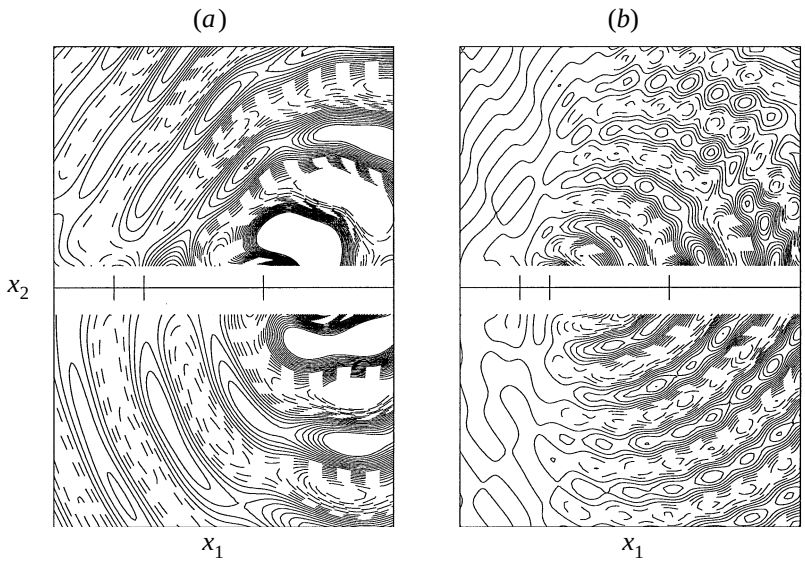

FIGURE 6. Acoustic field (dilatation) predicted from the acoustic analogy with the simplified source term of equation (4) for (*a*) $f/4$, (*b*) $f/2$. Contour levels (all times 10^6): (*a*) -1.0 to 1.0 at intervals of 0.1; (*b*) -0.4 to 0.4 at intervals of 0.04.

frequencies), are determined by

$$\hat{\Pi}_n(x_1, x_2) = \int_{-\omega_n/(1+M_2)}^{\omega_n/(1-M_1)} (\omega_n + Uk)\phi_n(k, x_2)\mathrm{e}^{2\pi \mathrm{i} k x_1}\,\mathrm{d}k, \tag{15}$$

and

$$\hat{\Theta}_n(x_1, x_2) = 2\pi \mathrm{i} \int_{-\omega_n/(1+M_2)}^{\omega_n/(1-M_1)} (\omega_n + Uk)^2\phi_n(k, x_2)\mathrm{e}^{2\pi \mathrm{i} k x_1}\,\mathrm{d}k, \tag{16}$$

respectively. Note that the infinite limits on the integration have been replaced by $-\omega_n/(1+M_2)$ and $\omega_n/(1-M_1)$, since for larger values of k, ϕ_n decays exponentially in $\pm x_2$. Thus the solution found will only be valid outside the mixing region where the exponential terms will have decayed significantly. Note also that when the pressure fluctuations are small the logarithmic pressure fluctuation Π' is equivalent to the regular pressure fluctuation, p'. The integrals are once again computed using numerical quadrature as discussed by Colonius *et al.* (1995). The far-field directivity can also be determined asymptotically from equations (15) and (16) for large $r = (x_1^2 + x_2^2)^{1/2}$ using the method of stationary phase; the details of the asymptotic analysis are straightforward and are given in Colonius *et al.* (1995).

3.2. *Comparison of acoustic analogy predictions and DNS*

The results of the acoustic analogy predictions are found using the simplified source term equation (4). The acoustic analogy is solved as discussed in the previous section. Note that the source is sampled every 22 time steps from the DNS data and its DFT is taken using the method described in the Appendix. The results of the computation are shown in figure 6, where the predicted dilatation outside the mixing region is plotted for frequencies $f/2$ and $f/4$.

Comparing figure 6 with the results from the DNS (figure 5*a*,*b*), it is evident that the acoustic analogy predictions agree quite well with the acoustic fields directly measured

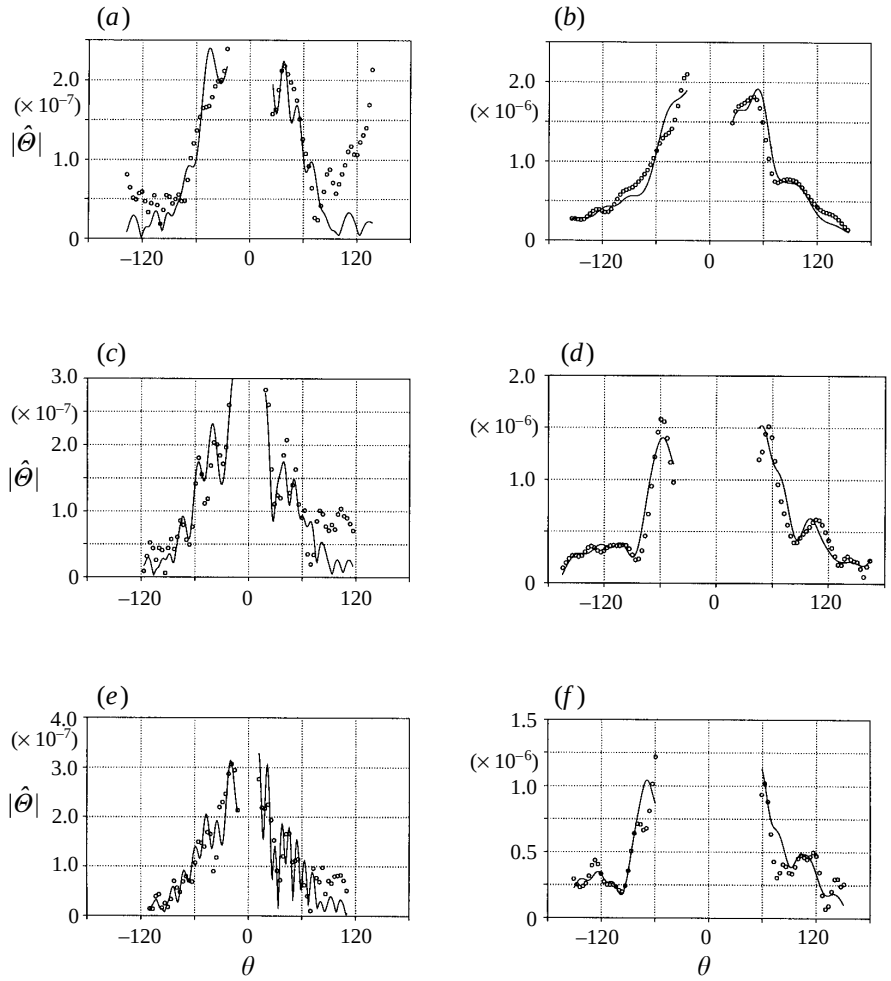

FIGURE 7. Comparison of the magnitude of the acoustic waves (dilatation) predicted by solving the acoustic analogy (solid lines) with the simplified source of equation (4) and from the DNS (open circles). Refer to figure 8 for the locations in the computational domain from which the above data are taken. (*a*) $f/2$, $r = 100.0$; (*b*) $f/4$, $r = 100.0$; (*c*) $f/2$, $r = 150.0$; (*d*) $f/4$, $r = 150.0$; (*e*) $f/2$, $r = 200.0$; (*f*) $f/4$, $r = 200.0$.

from the DNS. One exception is near the inflow boundary where spurious waves are created by the boundary conditions in the DNS. To aid in a more quantitative comparison of the acoustic fields from the DNS and the acoustic analogy, the predictions are replotted in figure 7. The magnitude of the dilatation is plotted along arcs at various distances from the saturation point for the instability wave corresponding to the particular frequency plotted, i.e. $x_1 = 75$ for frequency $f/2$ and $x_1 = 175$ for frequency $f/4$. We pick this saturation point as the 'apparent origin' of the waves. Figure 8 shows a diagram of the computational domain with the locations from which the data in figure 7 are taken. Note that the DNS and acoustic analogy field are not plotted for $|x_2| < 40.0$ in the plots since it is impossible to distinguish between the acoustic waves and the near-field dilatation in the DNS. Also, since the acoustic fields from the DNS at other frequencies were found to be contaminated by

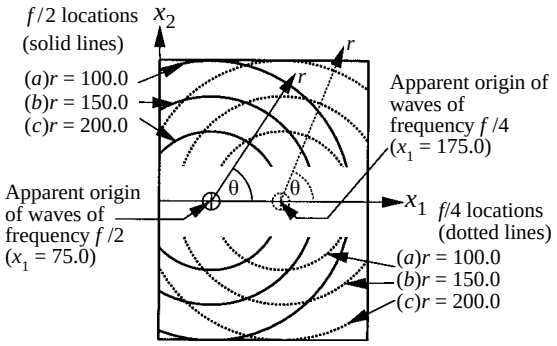

FIGURE 8. Diagram of computational domain showing the locations for the curves plotted in figure 7.

boundary condition errors, and are anyway very much smaller than those at $f/2$ and $f/4$, the acoustic analogy predictions for those frequencies are not presented.

Very little decay with increasing r is evident in the magnitude of the acoustic waves in figure 7. Apparently the waves have not reached their asymptotic far field (where their amplitude should decay like $r^{-1/2}$) which is not surprising since there are only 1 to 4 wavelengths (depending on the frequency and observation angle θ) of the generated sound inside the computational domain.

While the acoustic analogy predictions are in good agreement with the DNS, we point out that the very small differences in the manner in which the source terms were computed (specifically the DFT of the sources) led to large variations in the predicted acoustic field. The computational details of the sensitivity are specific to the methodology of the present analysis and may not be of interest to the general reader. Details about the sensitivity of the prediction are therefore placed in the Appendix. In §3.6 evidence is given that connects the sensitivity of the numerics with the presence of flow–acoustic interaction terms in the source.

3.3. *The full form of the source term*

The acoustic fields generated by those parts of the full source which are neglected in arriving at the simplified source of equation (4) are now examined. Given that the predictions based on the simplified source are in good agreement with the DNS, it would appear that the remainder of the terms should (together) produce a negligible acoustic field. This is verified in figure 9, where the acoustic field (at the first subharmonic frequency, $f/2$) produced the by full source, equation (3), is compared to the acoustic field produced by the simplified source, equation (4). The two predictions are very nearly identical, indicating that the total contribution of terms II–V in equation (3) are negligible. The same conclusion holds for frequency, $f/4$, but the figures have been omitted for the sake of brevity.

The acoustic fields produced by each of the neglected terms (IIa,b, IIIa,b, IVa,b and Va,b) are shown in figure 10 at the same contour levels as figure 9. The sum of all these terms is also plotted (figure 10*a*). For terms IIIa and IIIb only the zero crossings of the waves can be seen in the plot, and thus the amplitude is more than an order of magnitude smaller than amplitude of the acoustic waves generated by the total source. Terms Va and Vb individually have a slightly more significant amplitude, amounting to about 20% of those from the full source. But they are nearly equal in amplitude and of opposite phase – thus their total contribution is negligible.

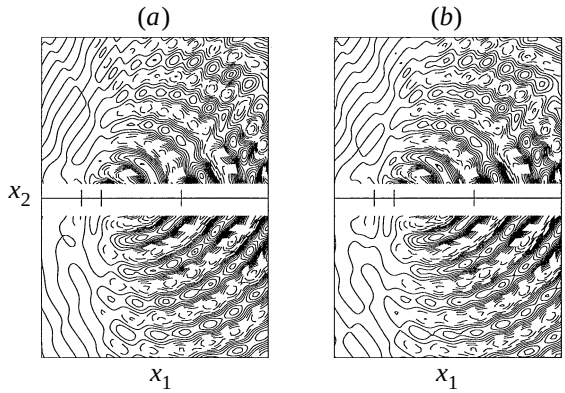

FIGURE 9. The acoustic field at frequency $f/2$ predicted by acoustic analogy with: (*a*) the full source term (equation (3)), and (*b*) the simplified source, terms Ia and Ib only (equation (4)). Contour levels for all plots (all times 10^6): -0.4 to 0.4 at intervals of 0.04.

On the other hand, terms IIb and IVa and IVb are not negligible individually. Each generates an acoustic field of the same order of magnitude as the full source. Moreover, the conclusions are very similar for the acoustic field at frequency $f/4$.

In Goldstein's (1976*a*) derivation of equation (4), term II of equation (3) has been neglected because it is proportional to the dilatation and thus, for low Mach number, it should be (and, in fact, is) significantly smaller than term I. Terms III–V of equation (3) contain Π', and arise from the linearization of the left-hand side of equation (1). Interpreting Π' as the solution of the acoustic analogy, Goldstein (1976*a*) concludes that these terms arise from scattering of the sound by the flow. Neither of the two arguments can be strictly correct because parts of terms II and IV individually produce acoustic fields which are quite intense compared to the total.

A better justification for neglecting terms II, IV and V is actually provided in a later paper by Goldstein (1984), though in a different context. In this later work Goldstein derives equation (4) by performing a perturbation expansion about a transversely sheared parallel mean flow, rather than by the acoustic analogy approach used here. In that case, to first order, the solution for disturbances in the flow is given by the solution of equation (2) with the Γ set to zero. These solutions are then taken as the 'first order' solutions and the equations are written to second order in the deviations of the pressure from its uniform value in the base flow. The second-order equation is essentially equation (4), but with a few important differences. The source term only contains the 'first order' interactions. That is the primed quantities are no longer the deviations of the flow from the parallel base flow, but are, in fact, the 'first order' disturbances. Therefore term V (which contains only triple products) is not included in the second-order equation, but rather would appear as a source in the equation at third order. Then Goldstein (1984) cleverly rewrites the second-order equation in terms of a new dependent variable $\Pi_2 - \frac{1}{2}(\gamma - 1)\Pi_1^2$, where the subscript here refers to the order of the quantity. Since the first-order pressure, Π_1, has no acoustic field when the flow is subsonic (Goldstein 1984) the new variable is equivalent to the second-order pressure in the far field. The source term for the new dependent variable, $\Pi_2 - \frac{1}{2}(\gamma - 1)\Pi_1^2$, however, does not contain terms II and IV.

Now, since the source is computed from the DNS data, it is impossible to decompose the total velocities and pressure into first-order, second-order, etc. quantities. However,

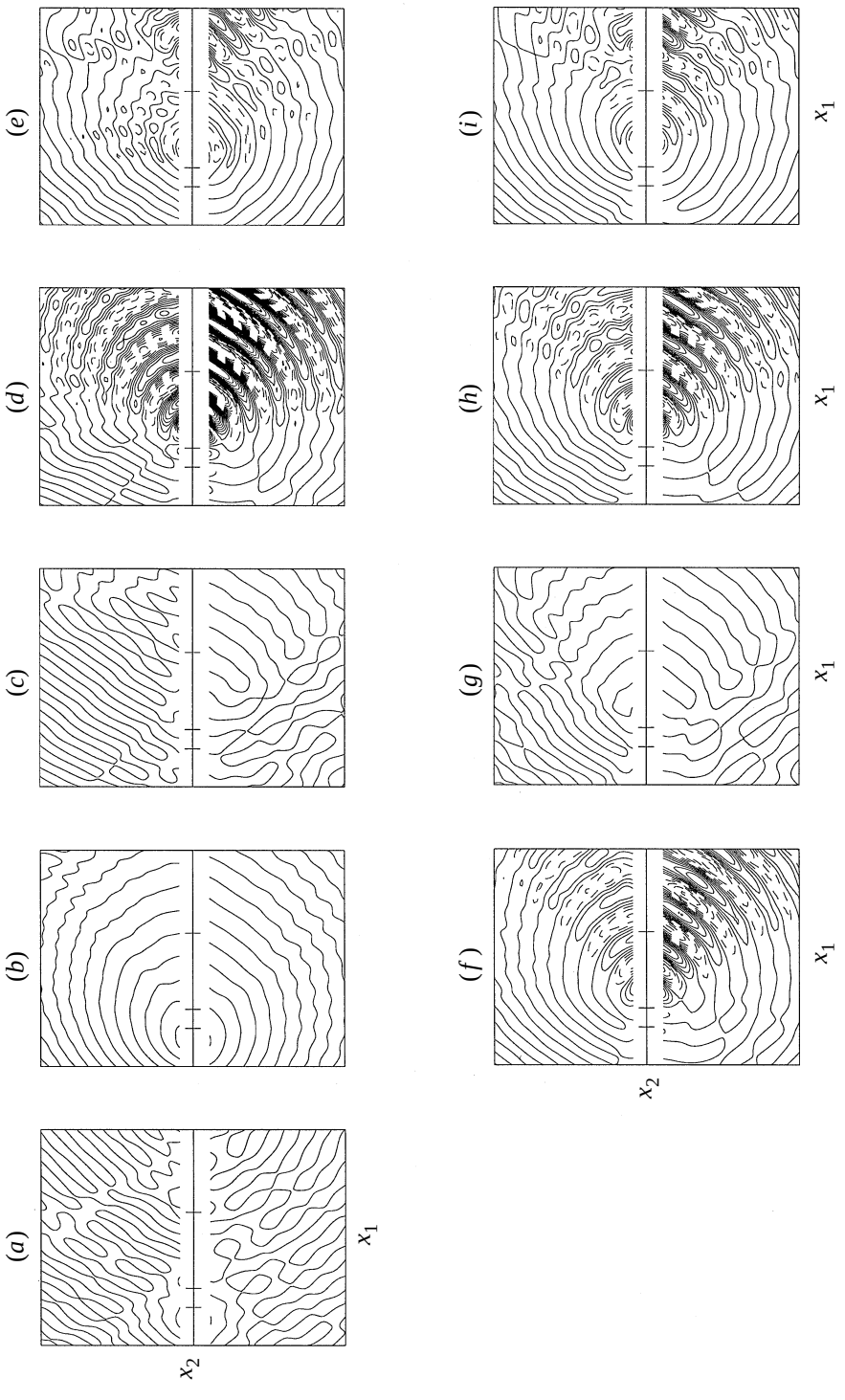

FIGURE 10. The acoustic field predicted by the acoustic analogy with individual components of the full source. The contour levels are the same as in figure 9. (*a*) Sum of terms II–V, (*b*) term IIa, (*c*) term IIIa, (*d*) term IVa, (*e*) term Va, (*f*) term IIb, (*g*) term IIIb, (*h*) term IVb, (*i*) term Vb.

it is possible to write an equation for the square of Π':

$$\mathscr{L}(\tfrac{1}{2}\Pi'^2) = \tilde{\Gamma} = \frac{\mathrm{D}_o}{\mathrm{D}t}\Bigg(\underbrace{\frac{\partial u_i'}{\partial x_i}\frac{\partial u_k'}{\partial x_k}}_{\text{Term IIa}} \underbrace{-a^2\frac{\partial \Pi'}{\partial x_i}\frac{\partial \Pi'}{\partial x_i}}_{\text{Term IVa}}\Bigg) - 2\frac{\mathrm{d}U}{\mathrm{d}x_2}\Bigg(\underbrace{\frac{\partial u_2'}{\partial x_1}\frac{\partial u_k'}{\partial x_k}}_{\text{Term IIb}} \underbrace{-a^2\frac{\partial \Pi'}{\partial x_1}\frac{\partial \Pi'}{\partial x_2}}_{\text{Term IVb}}\Bigg) + \cdots \tag{17}$$

where the dots refer to terms which are triple products similar in form to term V of Γ, and $\mathscr{L}$ is the linear wave operator of equation (2). Equation (17) follows (after some tedious algebra) from equations (2) and (3). Now, adding equations (17) and (2) gives

$$\mathscr{L}\big(\Pi' + \tfrac{1}{2}\Pi'^2\big) = \tilde{\tilde{\Gamma}} = \Gamma + \tilde{\Gamma}, \tag{18}$$

The source $\tilde{\tilde{\Gamma}}$ of equation (18) will consist solely of terms I, III, and terms which are triple products of the primed variables. And in the far field $\Pi' + \frac{1}{2}\Pi'^2$ will be indistinguishable from Π' since the acoustic field has very small amplitude. This leads to the conclusion that the sum of terms II, IV, and V in Γ produces an acoustic field which can be regarded as a 'higher order' approximation in a perturbation expansion of the flow. Finally, note that the preceding arguments apply equally well to the second subharmonic frequency, $f/4$, which has been omitted for the sake of brevity.

3.4. *The structure of the source terms and their asymptotic far-field radiation*

The asymptotic far-field directivity is determined, as noted in §3.1, by using the method of stationary phase to evaluate the inverse Fourier transform of the acoustic analogy solutions for large $r = \left(x_1^2 + x_2^2\right)^{1/2}$. In figure 11 the acoustic pressure (multiplied by $r^{1/2}$) in the asymptotic far field at frequencies $f/2$ and $f/4$ is plotted against the angle between the observation point at a distance r from the source and the positive x_1-axis. Note that for large r, information about the actual source position for the waves is lost, and therefore r is taken as the distance from $x_1 = x_2 = 0$. The directivity shown in figure 11 is complicated, but overall is strongly peaked for angles $-90^\circ < \theta < 90^\circ$, attaining a global maximum near $\theta = -30^\circ$. Unlike the directivity from a jet, which is expected to be symmetric about $\theta = 0$, the directivity is weaker for $\theta > 0$. Furthermore, the maximum directivity occurs at a cusp. Such cusps are the result of the difference in velocity on either side of the layer, causing certain spatial harmonic components (at a particular frequency) to radiate to one side of the layer only (they are evanescent waves on the other side). These cusps have been seen in simple acoustic models of sources near vortex sheets (Gottlieb 1960; Ffowcs Williams 1974). For $M_1 = 0.5$ and $M_2 = 0.25$ it can be shown that the cusps occur at angles $\theta = -30^\circ$ and $\theta = 117^\circ$ in the low- and high-speed streams respectively (Colonius *et al.* 1995).

In addition to the overall trends, the directivity also contains smaller-scale oscillations such as occur when a wave field is significantly scattered. In fact, for frequency $f/2$ the directivity is highly oscillatory and qualitatively resembles the directivity for low-frequency waves which are scattered by a single vortex (see, for example, figure 5 of Colonius *et al.* 1994).

Consider now the far field which would be generated by a compact quadrupole source of the form of equation (4). The directivity produced by low-frequency *convecting point sources* in jets has been computed using equation (2) with the source given by equation (4) (or something very similar) by Goldstein (1975, 1976*b*), Tester & Morfey (1976), and Balsa (1977); solutions in the high-frequency limit are given by Tester & Burrin (1974), Balsa (1976, 1977), Tester & Morfey (1976), and Goldstein

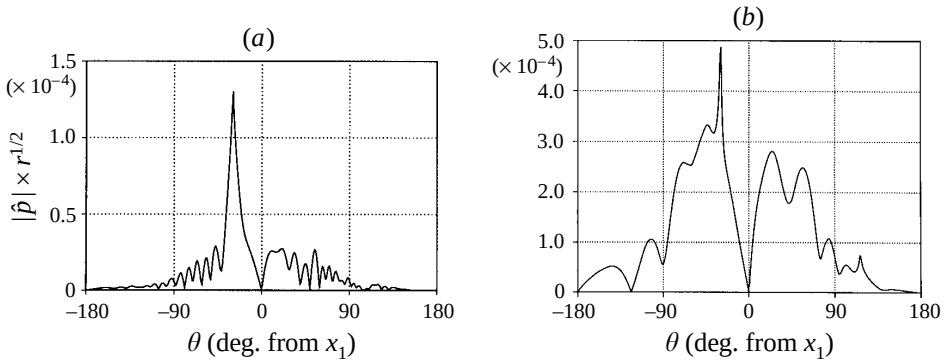

FIGURE 11. The asymptotic far-field directivity. (*a*) $f/2$, (*b*) $f/4$.

(1982) and others; full solutions are given for the special case of plug flow by Mani (1976). These computations are reviewed by Goldstein (1984).

For low frequency, Goldstein (1975, 1976*b*) and others use equation (4) with $u_i'u_j'$ modelled by

$$u_i'u_j' = A_{ij}\exp(2\pi i\omega t)\delta(x_1 - Ct)\delta(x_2), \tag{19}$$

where A_{ij} is a tensor of constants, and C is a constant convection velocity. Specifically, Goldstein (1975, 1976*b*) has shown that for convecting sources, Doppler factors, $(1 - C\cos\theta)^{-n}$ with n as high as 5, can multiply the directivity and thus produce a highly directive acoustic field. This is in accord with experimental observations. Similarly, Ffowcs Williams (1974), and later Dowling *et al.* (1978) have shown that the directivity associated with compact convecting quadrupole sources is modified by proximity to a vortex sheet, causing a more highly directive acoustic field and a zone of silence along the shear layer axis due to refraction by the vortex sheet, similar to that which exists in the current acoustic field (see figure 11).

In the present flow which is nearly periodic in time, the sources are stationary and the representation of the acoustic sources at a particular frequency as convecting disturbances is not appropriate. A stationary compact quadrupole source would, instead, be given by

$$u_i'u_j' = A_{ij}\exp(2\pi i\omega t)\delta(x_1)\delta(x_2). \tag{20}$$

To investigate the directivity associated with such sources in the mixing layer, the numerical scheme for solving equation (2) is used with a source of the form given by equation (20). In order to solve for the point source numerically, the delta functions in equation (20) must be replaced with sources of finite support. We choose the distribution

$$u_i'u_j' = A_{ij}\exp(2\pi i\omega t)\mathrm{e}^{-\pi(x_1/\epsilon_1)^2}\mathrm{e}^{-\pi(x_2/\epsilon_2)^2}/(\epsilon_1\epsilon_2). \tag{21}$$

In the limit as ϵ_1 and ϵ_2 both go to zero equation (21) approaches equation (20). By experimentation, it was found that for frequencies $f/2$ and $f/4$, a source with $\epsilon_1 = \epsilon_2 = 0.1$ is sufficiently compact such that the acoustic fields produced by each of A_{11}, A_{22} and A_{12} are identical to those which would be produced by equation (20). Figure 12 presents the directivity patterns for the point quadrupoles A_{11}, A_{22} and A_{12} with a frequency $f/2$ in a flow with mean streamwise velocity $U(x_2)$ which is taken as the real mean flow of the mixing layer at $x_1 = 0$. The pressure is normalized in each case by the corresponding strength of the source. The mean velocity and shear have a dramatic effect on the directivity. In comparison, the directivities of the compact

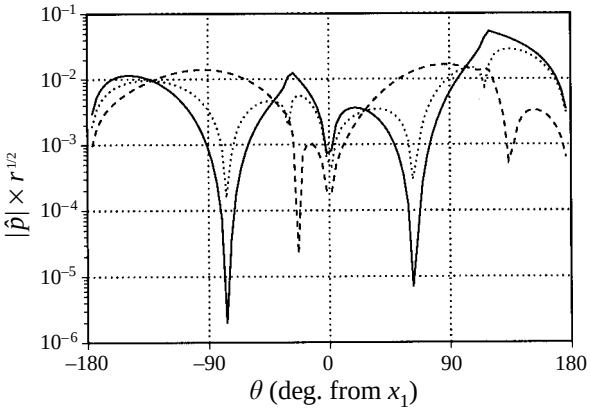

FIGURE 12. The far-field directivity of stationary point quadrupole sources in a mixing layer at frequency $f/2$ for the A_{11} component only (———); the A_{12} component only (·····); the A_{22} component only (– – – –).

sources in a quiescent media are $\cos^2\theta$, $\sin^2\theta$, and $\cos\theta\sin\theta$ for A_{11}, A_{22} and A_{12}, respectively. The mean flow causes the amplitude of the waves to be increased for waves propagating upstream (i.e. angles greater than 90°) and decreased for waves propagating downstream. Note that this is the Doppler effect, but for a stationary observer and stationary source in a flow (as opposed to a convecting source relative to a stationary observer in a flow, as considered by Goldstein (1975, 1976*b*)). For a stationary source the frequency of the source and observer are the same, but the waves propagating upstream have shorter wavelength and greater magnitude. This is opposite to the desired trend of greater amplitude in the downstream direction. Clearly it is difficult to imagine constructing the observed directivity (figure 11) from any linear combination of the point sources.

The acoustic field for the source in equation (21) with varying values of ϵ_1 and ϵ_2 has also been computed, and thus, to a limited extent, certain effects of source non-compactness have been considered. While there is a gradual trend towards attenuation of the directivity in the upstream direction as ϵ_1 and/or ϵ_2 are increased from 0.1, the effect is not of sufficient magnitude to explain the observed directivity of figure 11. At large values of ϵ_1 and/or ϵ_2 equation (21) merely gives an acoustic field which is beamed to $\pm 90°$.

In short, the directivity of the acoustic field produced by the vortex pairings is dissimilar to that which would be produced by a stationary compact quadrupole source. Many would argue that equation (4) is, by definition, a quadrupole source, albeit a possibly non-compact one. The utility of such a definition is unclear, given that the far field of a non-compact quadrupole is in principle no different from a non-compact monopole, dipole, etc. Further complicating the discussion of the acoustic field produced by terms Ia and Ib is the presence of flow–acoustic interactions in the source, which will be discussed in the next section.

Figure 13 shows part of the simplified source term $\partial^2 u_i' u_j'/\partial x_i x_j$ in the near field. Its real part, imaginary part and amplitude (in frequency space) are plotted for the frequencies $f/2$ and $f/4$. The source term for each frequency attains a maximum amplitude near the saturation point of the instability wave of that frequency ($x_1 \approx 75$ and $x_1 \approx 175$ for frequency $f/2$ and $f/4$ respectively, see figure 4). The source term has a very large extent in the x_1-direction, decaying very little by the end of the

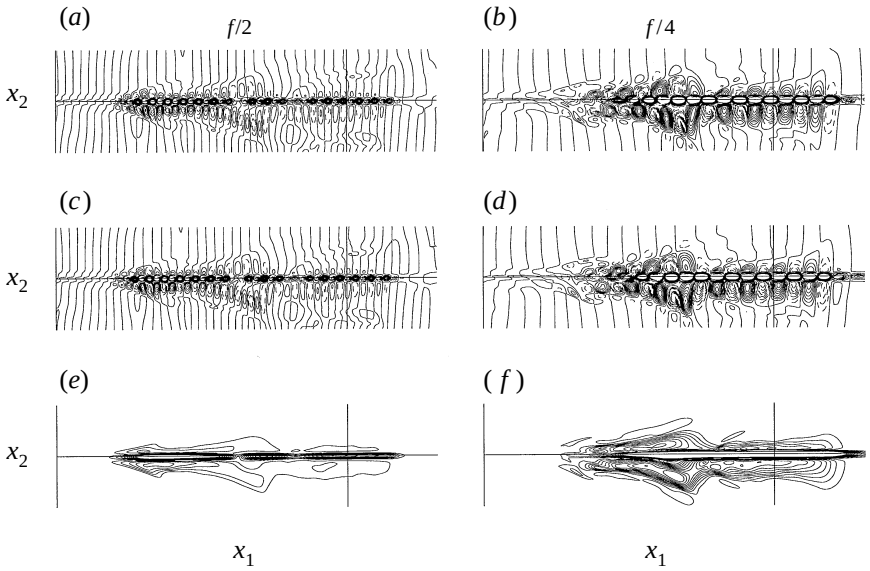

FIGURE 13. Isocontours of the real part (*a*,*b*), imaginary part (*c*,*d*), and magnitude (*e*,*f*) of the DFT of the quantity $\partial^2 u_i' u_j'/\partial x_i x_j$ at frequencies $f/2$ (a, c, e) and $f/4$ (b, d, f). A portion of the domain extending to $x_2 = \pm 10$ and $x_1 = 400$ is plotted, and the normal direction has been blown up by a factor of 5. The solid line at $x_1 = 285$ indicates the end of the 'physical' part of the computational domain. Dashed lines are negative contours and solid lines are zero and positive contours. Contour levels: (*a*), (*c*) and (*e*) -0.4×10^{-2} to 0.4×10^{-2} at intervals of 0.04×10^{-2}; (*b*), (*d*) and (*f*) -0.1×10^{-2} to 0.1×10^{-2} at intervals of 0.01×10^{-2}.

computational domain. Most of the decay occurs in the sponge region (downstream of the solid line in the plot which demarks the end of the 'physical' part of the computation, $x_1 = 285$, from the sponge). In the normal direction, the source term is quite concentrated near the centre of the layer, decaying rapidly for large $|x_2|$. Note that the x_2-axis has been expanded by a factor of 5 in the figure. The width (in the normal direction) of the source term at frequency $f/4$ is essentially double the width at frequency $f/2$. The real and imaginary parts of the source term show a very regular structure – they are approximately sinusoidal with the wavelength of the instability wave for the corresponding frequency. The real and imaginary parts are nearly identical but for a phase shift of $\pi/2$. Thus they are propagating wave packets whose amplitude grows and decays in x_1. Since the phase shift is so nearly constant, they propagate at a nearly constant speed, roughly the phase velocity for the instability waves, $M \approx 0.4$, for both frequencies. The data from figure 13 are replotted in figure 14 along the centreline, $x_2 = 0$, to show the wave structure of the source terms more clearly.

Note that the while the acoustic waves produced at the pairing frequencies appear to emanate from a small region near the saturation locations, the source terms are not highly concentrated near those points – they do not resemble point sources. Since they have the form of a modulated wave packet their energy is largest at the wavenumber of the instability wave at the corresponding frequency. This wavenumber is well outside the range of wavenumbers for which acoustic waves are radiated to the far field, given by equation (13).

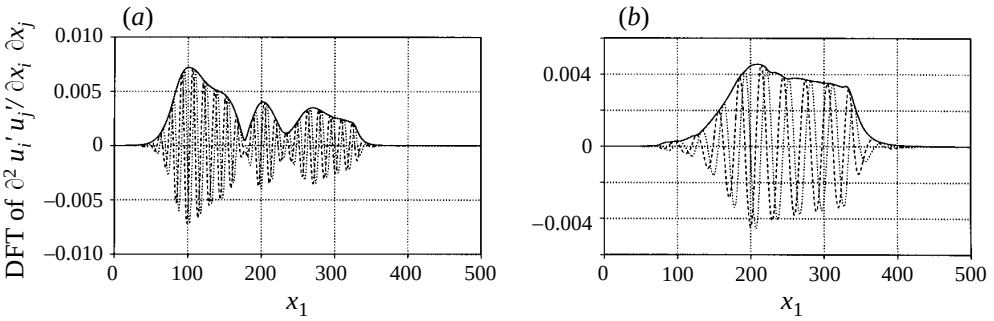

FIGURE 14. The DFT of $\partial^2 u_i' u_j'/\partial x_i x_j$ versus x_1 at $x_2 = 0$ for frequencies (*a*) $f/2$ and (*b*) $f/4$. ····· Real part; – – – – imaginary part; ——— magnitude.

3.5. *Comparison with superdirective acoustic fields*

What is clearly missing from the compact quadrupole source of equation (20) is a term which would account for the modulated wave packet structure of the sources in the x_1-direction. The actual source structure is the consistent with the 'superdirective' source considered by Crighton & Huerre (1990, hereafter referred to as CH). A simplified situation is considered by CH, where the two-dimensional acoustic field is found for a pressure disturbance at $x_2 = 0$ having the form of a modulated wave packet in x_1. Specifically, the pressure at $x_2 = 0$ is modelled as:

$$p(x_1, 0, t) = A(x) \exp(2\pi i k_0 x) \exp(2\pi i \omega t), \tag{22}$$

where $A(x)$ is the envelope function, and k_0 is the wavenumber of the modulation, equal, approximately, to the wavenumber of the instability wave at frequency ω. The resulting acoustic far field has a directivity of the form

$$|\hat{p}| \sim \sin\theta e^{aM_c \cos\theta}, \tag{23}$$

for an $A(x)$ whose Fourier transform decays exponentially fast for large k. The constant a is related to the overall width of the envelope function compared to the acoustic wavelength, and M_c is the phase speed of the pressure disturbance at $x_2 = 0$, i.e. $M_c = \omega/k_0$.

The pressure from the DNS at $x_2 = 0$ is plotted in figure 15 and conforms to equation (22). The Fourier transform of the pressure is plotted as a function of k/ω for $f/2$ and $f/4$ in figure 16, and except for a spike in the transform very near $k = 0$, the transform is decaying rapidly in the range of wavenumbers which can radiate acoustic waves to the far field, $-0.8 < k/\omega < 2$. Though the shape of the envelope function is more complicated than those considered by CH, the transform for large $|k - k_0|$ decays at a rate which can be roughly approximated by an exponential function, as depicted in the plot. The sharp spike near $k = 0$ is due to slight overall drift in the pressure mentioned in §2.3. It does not appear to have any significant consequence on the results given below.

We modify the stationary-media model given by CH, to take account of the mean flow in the mixing layer. The term $M_c \cos\theta = (\omega/k_0)\cos\theta$ in equation (23) arises from the radiation of a particular wavenumber, k, according to its stationary phase relation $k = -\omega\cos\theta$, in a stationary medium. The convection velocities on either side of the layer can be accounted for by modifying the exponential term arising in

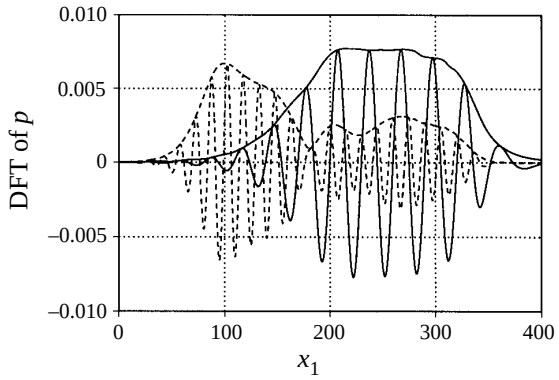

FIGURE 15. The DFT of p at $x_2 = 0$ for $f/2$ (– – – –) and $f/4$ (———). The real part and magnitude are shown – the imaginary part is similar to the real part in each case but shifted in phase by $\pi/2$.

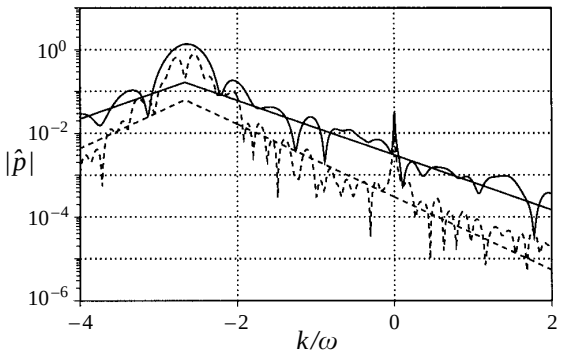

FIGURE 16. The magnitude of the Fourier transform in x_1 of the DFT of p at $x_2 = 0$ for $f/2$ (– – – –, $\epsilon = 0.05$) and $f/4$ (———, $\epsilon = 0.08$). The straight lines and values of ϵ correspond to an exponential decay given by equation (24).

the Fourier transform of the pressure at $x_2 = 0$:

$$|\hat{p}| \sim \exp(-2\pi|k_{sp} - k_0|/\epsilon), \tag{24}$$

where $\hat{p}$ is the Fourier transformed pressure at $x_2 = 0$, ϵ is a small number, related to a and thus the width of the envelope function. The stationary point for the mixing layer is (Colonius *et al.* 1995)

$$k_{sp} = \begin{cases} \dfrac{\omega_n}{1 - M_1^2}\left(M_1 - \dfrac{\cos\theta}{(1 - M_1^2\sin^2\theta)^{1/2}}\right) & \text{if } 0 < \theta < \pi \\ \dfrac{\omega_n}{1 - M_2^2}\left(M_2 - \dfrac{\cos\theta}{(1 - M_2^2\sin^2\theta)^{1/2}}\right) & \text{if } -\pi < \theta < 0\ . \end{cases} \tag{25}$$

Note that when $M_1 = M_2 = 0$, equation (25) reduces to $k = -\omega\cos\theta$.

The constant ϵ is related to the width of the envelope function, and is determined from the DNS data by forcing the exponential term in equation (24) to pass through the Fourier transform of the pressure at $x_2 = 0$, again ignoring the spike near $k = 0$. These curves are shown in figure 16 along with the Fourier transform of the pressure at $x_2 = 0$. The exponential function captures the overall trend of the transformed pressure with $\epsilon = 0.08$ for frequency $f/4$ and $\epsilon = 0.05$ for frequency $f/2$. Note that

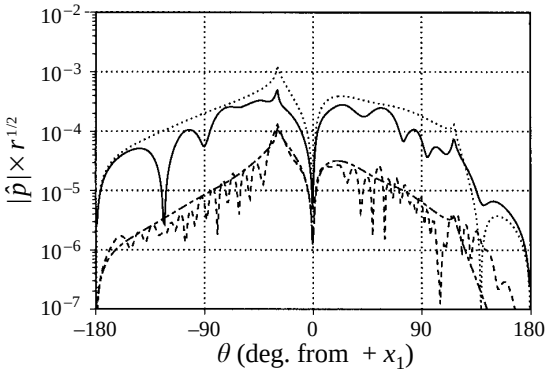

FIGURE 17. The asymptotic far-field directivity resulting from: the full source at $f/4$ (———); the modelled directivity at $f/4$ (·····); the full source at $f/2$ (– – – –); and the modelled directivity at $f/2$ (— – —).

for both frequencies, $1/\epsilon$ is about a quarter of the acoustic wavelength at $\theta = \pm 90^\circ$ to the source.

It is more difficult to account for the shearing by the mean flow. First, the model proposed by CH has no structure in the x_2-direction. The acoustic waves are assumed to be forced by the pressure at the centreline of the layer. The dipole-like term, $\sin\theta$, in equation (23) will surely be modified by the shear in a manner similar to the quadrupole components A_{ij} discussed above. Here we correct for shear in the $\sin\theta$-term of equation (23) in an *ad hoc* way by finding the directivity for a stationary dipole (aligned with the x_2-axis) in the present shear flow and multiply that directivity by the superdirective factor equation (24).

To ascertain the form of this modified dipole directivity equation (2) is solved with Γ replaced by a dipole source of the form

$$\Gamma = \frac{\mathrm{D}_o^2}{\mathrm{D}t^2}\left[\exp(2\pi \mathrm{i}\omega t)\frac{\partial}{\partial x_2}\left(\mathrm{e}^{-\pi(x_1/\epsilon_1)^2}\mathrm{e}^{-\pi(x_2/\epsilon_2)^2}\right)/(\epsilon_1\epsilon_2)\right], \tag{26}$$

where, as in equation (21), ϵ_1 and ϵ_2 control how compact the dipole is. This is the form of a dipole mass source inserted into the equations of motion. Note that equation (21) should not be interpreted as a source model – it is only used to determine how shear might be accounted for in the $\sin\theta$-term of equation (23).

The resulting directivity (i.e. the product of modified dipole-like factor given by the acoustic field produced by equation (26) and the superdirective factor of equation (24)) is plotted figure 17. The directivity of the present mixing layer (figure 11) is replotted in figure 17 for comparison. The agreement, while quantitatively inaccurate, captures the overall trends of the directivity including the cusps and the asymmetry in the directivity. Note that $\epsilon_1 = 0.01$ has been used for both frequencies and the less compact values of $\epsilon_2 = 1$ and $\epsilon_2 = 2$ are used for frequencies $f/2$ and $f/4$ respectively; the results are not very sensitive to the value of ϵ_2 (unless ϵ_2 is much larger than 1). The values of ϵ_1, ϵ_2, and the overall amplitude of the directivity used were chosen to produce the best agreement with the computations. The main point is that the directivity produced by the vortex pairings is similar to that which would be produced by superdirective sources in a shear flow.

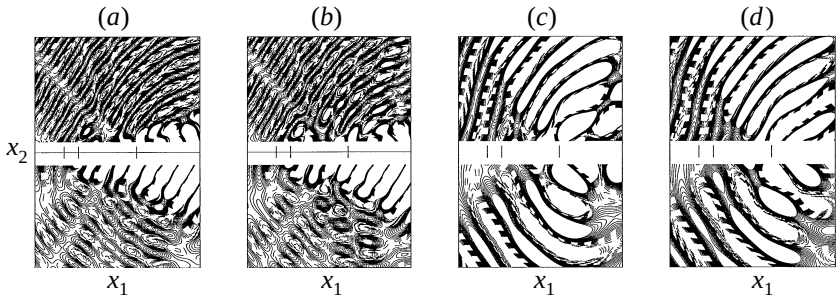

FIGURE 18. The acoustic field predicted by the acoustic analogy with individual components of the full source: (*a*) $f/2$, Term Ia; (*b*) $f/2$, Term Ib; (*c*) $f/4$, Term Ia; (*d*) $f/4$, Term Ib. Contour levels (all times 10^6): (*a*, *b*) -0.4 to 0.4 at intervals of 0.04; (*c*, *d*) -1.0 to 1.0 at intervals of 0.1.

3.6. *The effects of flow–acoustic interaction*

Consider the acoustic fields produced individually by the two important parts of the overall source term, i.e. terms Ia and Ib. The acoustic fields produced by each of the two terms individually at both subharmonic frequencies are plotted in figure 18, and should be compared to the acoustic fields produced by the total source (figures 6*b*, and 6*a* for frequencies $f/2$ and $f/4$, respectively). Both parts of term I produce an acoustic field with a magnitude which is significantly larger than that produced by their sum. The fields produced individually by terms Ia and Ib at $f/2$ make very large contributions to the acoustic field which emanates from the region downstream of the second pairing, unlike their sum which appears to radiate waves predominately from the region of the first pairing. Compact quadrupole sources arise from a cancellation between two opposing dipole sources, but it is difficult to imagine why the acoustic field produced by the flow in the region of the first pairing should be the produced by two large but mutually cancelling sources in an entirely different region of the flow. More likely, there is another reason, apart from any multipole nature of the sources, for such a cancellation.

In fact, parts of the large nearly cancelling acoustic fields produced by terms Ia and Ib individually (downstream of the pairing) are due to the presence of so-called flow–acoustic interactions in the source terms (specifically terms which are linear in the perturbations to the true mean flow). The primed quantities in equation (4) are defined as departures from the parallel base flow, $U(x_2)$, and therefore the products of primed quantities in equation (4) in reality contain terms which are linear in the true fluctuations of the flow about its true mean. To accertain the effects of such terms, we recompute equation (4) from the DNS data as follows. Let the true mean (time average) velocities be given by $\bar{u}_i$ and the fluctuations about the mean by $\tilde{u}_i$. Then equation (4) can be written

$$\Gamma \approx \frac{\mathrm{D}_o}{\mathrm{D}t}\Bigg(\underbrace{\frac{\partial^2 \tilde{u}_i \tilde{u}_j}{\partial x_i x_j}}_{\text{Term A}}\Bigg) - 2\frac{\mathrm{d}U}{\mathrm{d}x_2}\underbrace{\frac{\partial^2 \tilde{u}_2 \tilde{u}_j}{\partial x_1 x_j}}_{\text{Term B}} \tag{27}$$

where we have neglected all terms linear in the true fluctuations (i.e. products of the true fluctuations and the mean flow or the parallel base flow). Equation (27) is consistent with past interpretations of the primed quantities in equation (4) as being turbulent fluctuations (see, for example, the discussion on page 282 of Goldstein 1984). Note that equation (27) together with equation (2) is no longer 'exact'. This

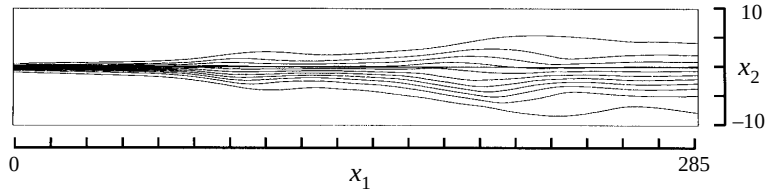

FIGURE 19. Mean streamwise velocity contours in near-field mixing region. The normal axis is expanded by a factor of 2.5. Contour levels: min: 0.26, max: 0.49, increment: 0.023.

implies that the choice of the parallel base flow velocity, $U(x_2)$, which appears in both equations (27) and (2) is no longer arbitrary. That is, different choices of $U(x_2)$ change the linear terms which are neglected in writing the source in the form of equation (27).

We now examine the acoustic field produced by the source of equation (27), with different choices of $U(x_2)$. $U(x_2)$ is chosen to correspond to the true mean streamwise velocity of the layer, but at different positions in the layer. In figure 19, the contours of the mean streamwise velocity, $\bar{u}_1(x_1, x_2)$, are shown in the near-field region of the mixing layer. Near the locations where the pairings take place, the thickness of the layer essentially doubles. Thus, for example, the acoustic waves produced by the first pairing are radiated downstream into a flow with a significantly different mean streamwise velocity profile than that which exists at $x_1 = 0$ where $U(x_2)$ was previously defined.

In figure 20, the acoustic field at frequency $f/2$ which results from the source given by equation (27) with two different choices for $U(x_2)$ is plotted. In figure 20(*a*) $U(x_2)$ is set equal to $\bar{u}_1(0, x_2)$ (which is the value of $U(x_2)$ which was used in conjunction with the source of equation (4) in obtaining the acoustic field shown in figure 6*b*). The agreement with the DNS (figure 5*b*) is not very good, and there appear to be some spurious waves emanating from the region downstream of the pairing. In figure 20(*d*) the acoustic field is computed using the source of equation (27), but with $U(x_2)$ is set equal to $\bar{u}_1(100, x_2)$, which is near the apparent origin of the acoustic waves for frequency $f/2$. At $x_1 = 100$, the thickness of the layer has approximately doubled from its value at $x_1 = 0$. This field is in good agreement with both the prediction obtained from the source of equation (4) (figure 6*b*), and with the DNS result (figure 5*b*).

Thus the quadrupole source term of equation (4) can reasonably be interpreted as due solely to fluctuations about the true mean flow, so long as $U(x_2)$ is chosen to conincide with correct mean flow near the apparent origin of the waves. This is consistent with the idea of assuming that the mean flow is spreading slowly and can be considered as 'locally parallel'. Note that the acoustic field is not *very* sensitive to the choice of $U(x_2)$ so long as the chosen $U(x_2)$ is not too different from the true mean flow in the vicinity of the apparent source of the waves. In the context of the present results this means that for the waves emanating from the first pairing, reasonable predictions can be obtained when $U(x_2)$ is chosen from streamwise locations in the layer where the thickness is essentially double that of the initial thickness (i.e. from about $x_1 = 90$ to $x_1 = 180$).

In figure 20, the acoustic fields for the two different choices of $U(x_2)$ are also decomposed into their contributions produced individually by the two parts of overall quadrupole source term, terms A and B of equation (27). When $U(x_2) = \bar{u}_1(0, x_2)$ (which gives a total field in poor agreement with the DNS) the individual contributions

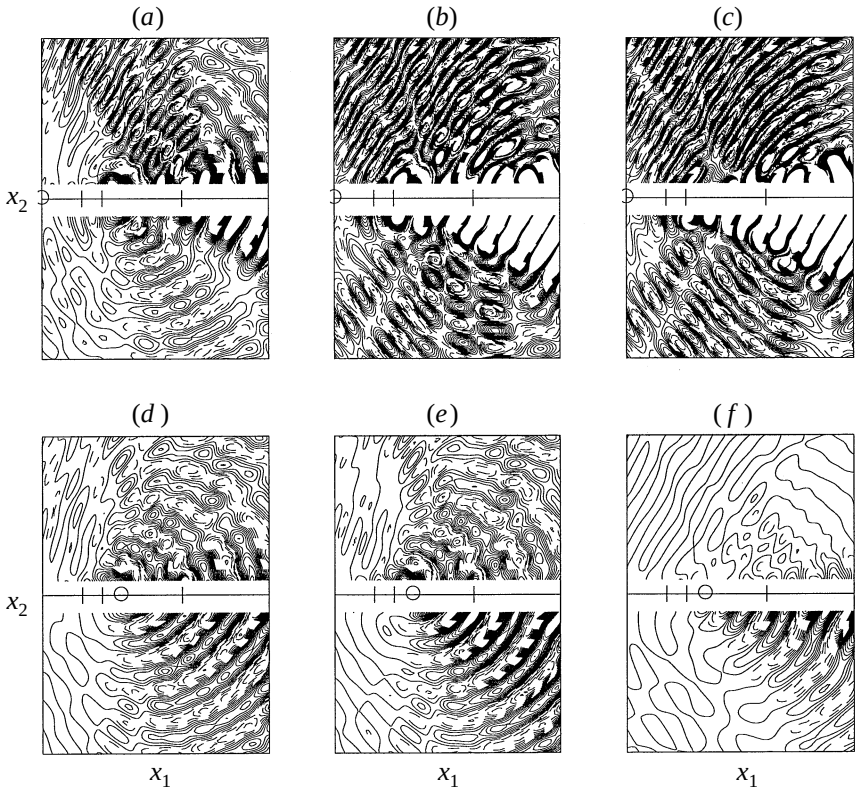

FIGURE 20. The acoustic field predicted by the acoustic analogy with the source given by equation (27), with different choices for $U(x_2)$: (*a*) total source with $U(x_2) = \bar{u}_1(0, x_2)$; (*b*) term A with $U(x_2) = \bar{u}_1(0, x_2)$; (*c*) term B with $U(x_2) = \bar{u}_1(0, x_2)$; (*d*) total source with $U(x_2) = \bar{u}_1(100, x_2)$; (*d*) term A with $U(x_2) = \bar{u}_1(100, x_2)$; (*d*) term B with $U(x_2) = \bar{u}_1(100, x_2)$. The circles on the x_1-axis indicate the location where $U(x_2)$ is taken to be equal to the mean streamwise velocity. Contour levels (all times 10^6) for all plots: -0.4 to 0.4 at intervals of 0.04.

from terms A and B are significantly larger than the total field, largely cancel one another, and appear to emanate from a region of the flow downstream of the second pairing. This is similar to the situation arising when the source given by equation (4) is used (figure 18*a*,*b*). By contrast, when $U(x_2)$ is chosen as the true mean flow near the apparent origin of the waves, the two contributions to the acoustic field from terms A and B (figure 20*e*,*f*) are similar in magnitude to the total and appear to emanate from the region of the flow near the vortex pairing. Here term B only modifies the acoustic field produced by term A at very shallow angles in the low-speed stream.

In summary, when the acoustic anology is 'exact' (as in figure 6), then the presence of products of the mean flow and fluctuations in terms Ia and Ib cause large but mutually cancelling acoustic fields. This gives good overall predictions for the acoustic fields, but can give misleading pictures of the individual contributions. When terms linear in the fluctuations are removed from the source terms, good overall predictions can be obtained, provided the appropriate base flow velocity, $U(x_2)$ is used.

As discussed in the Appendix, the solution to the acoustic analogy equation can be sensitive to the computational details of discrete Fourier transforming of the source. These sensitivities can, in fact, be traced entirely to the inclusion of linear terms in the source terms of equation (4). Though the total source equation (4) gives the

correct prediction, linear terms present in individual parts of the source create intense mutually cancelling acoustic fields as shown above. Thus small computational errors can easily upset the cancellation and yield large errors in the predicted acoustic fields.

From a computational point of view, the two main conclusions which can be drawn from the results of this section are that (i) if linear terms are neglected in the source terms, then the predicted acoustic field can be sensitive to the particular parallel flow velocity which is used in solving the acoustic analogy, and (ii) the presence of linear terms in the source leads to acoustic field predictions which are very sensitive to the details of the computation. Though it has been widely speculated that acoustic sources computed using DNS could exhibit such a sensitivity, it has usually been attributed to the idea of upsetting the 'multipole' cancellation of compact sources. Here such sensitivity arises when terms linear in fluctuations about the mean are lumped into the source term. This confirms the theoretical conclusion of Doak (1972) who proposed that an effective formulation of the acoustic analogy can only be obtained by extracting from the right-hand side all flow acoustic interaction terms.

4. Summary

The sound generated by vortex pairing in a compressible two-dimensional mixing layer which is forced to roll up into vortices and undergo two pairings has been investigated with DNS of the Navier–Stokes equations and with the acoustic analogy due to Lilley (1974). The source terms necessary to solve Lilley's acoustic analogy are determined from the DNS data. The predictions from the acoustic analogy are found to be in remarkably good agreement with the acoustic field from the DNS at the frequencies corresponding to the vortex pairings (these frequencies alone dominate the acoustic field), especially considering that the acoustic field is 4 to 5 orders of magnitude smaller (in amplitude) than the near-field fluctuations. Thus Lilley's equation has been validated in detail against a solution to the Navier–Stokes equations for the first time.

By considering the acoustic fields produced individually by the various terms in the full acoustic source for Lilley's equation, it was found that certain combinations of terms produced negligible acoustic fields. The negligible terms are identical to those Goldstein (1976*a*) neglected in arriving at a simplified quadrupole form of the source term (equation (4)). However, when taken individually, the neglected terms do not produce negligible acoustic fields. That is, some of the neglected terms produce large but mutually cancelling acoustic fields, and this indicates the need for caution in interpreting the relative importance of different terms in the acoustic source. Alternatively, it was shown, by analogy with the perturbation expansion for parallel shear flows considered by Goldstein (1984), that the neglected terms can, when taken in combination, be considered as producing only a 'higher-order' correction to the acoustic field.

The simplified source proposed by Goldstein (1976*a*, 1984) is of an appealing form because it extends the concept of Lighthill's (1952) quadrupole acoustic sources to parallel flows with mean shear. While the source term written in this form accounts for the observed acoustic field well, it was shown that the sources are not well modelled by compact quadrupole sources, despite the relatively low Mach number of the flow. In fact, the vortex pairings in the layer led to sources of the form of modulated wave packets in the streamwise direction. A model for a such a source (Crighton & Huerre 1990) was examined and the resulting 'superdirective' acoustic field compared favourably with the computations. It should be kept in mind, however, that the

present flow is one with no small-scale turbulence, and it is not well understood at present how the addition of small and random eddies to the large-scale vortices studied here will effect the modelling of the source terms.

Contributions to the source from products of the mean flow and fluctuations about the mean (the so-called flow–acoustic interaction terms) cause individual parts of the source to produce intense but mutually cancelling acoustic fields; small computational errors can upset this cancellation, giving rise to acoustic field predictions which are grossly in error, and small changes in the source terms can lead to misleading views of the relative importance of various terms. Therefore the present results point to the need for caution in applying acoustic analogies, for the good agreement between the direct computations and the acoustic analogy was only obtained provided that sufficient care was taken in processing the DNS data.

The authors are grateful to Professor Geoffrey Lilley for his helpful remarks on a draft of this paper. Part of this work was completed under grants ONR-N00014-88-K-0592 and ONR-N00014-92-J-1626 from the Office of Naval Research, while the first author was a graduate student at Stanford University. The first author is also grateful for recent support from the National Science Foundation under grant number CTS-9501349. Supercomputing time and support was provided by NASA-Ames Research Center and the Center for Turbulence Research. Some of the work presented here was presented in preliminary form in AIAA Paper 93-4328, CEAS/AIAA Paper 95-036, and ASME FED-Vol. 219.

Appendix A. Sensitivity of the acoustic analogy predictions

The acoustic analogy solutions of §3.2 require that the acoustic sources be discrete Fourier transformed in time. The DFT of a discrete time signal $F(t_j)$ is given by

$$\hat{F}_n = \frac{1}{N}\sum_{j=0}^{N-1} F(t_j)\mathrm{e}^{-2\pi \mathrm{i} jn/N}, \tag{A 1}$$

where $t_j = Tj/N$, and where T is the period of the transform. As noted in §2.2, the signal from the DNS is not perfectly periodic in time, but only nearly so. Thus error is introduced into the representation of the sources at a particular frequency.

When the power spectrum of a sampled function is desired, windowing techniques and averaging transforms of individual (overlapping) segments of the data may be used to increase the accuracy of the power spectrum in a particular frequency bin (see, for example, Press *et al.* 1992). In computing the frequency spectra of various quantities in the near field (including the acoustic sources), it was found (Colonius *et al.* 1995) that the values of the transformed quantities differed by as much as 5% (in amplitude) depending on which signal processing techniques were used. However, it was found that the value of the acoustic field predicted by solving the acoustic analogy varies by orders of magnitude depending on the particulars of the DFT computation. In particular none of the standard techniques (windowing, overlapping segments, etc.) gave agreement with the DNS results.

The key problem with the standard windowing techniques is that they are developed to attempt to 'resolve' the energy of both the periodic and aperiodic parts of a signal into nearby 'frequency bins'. They give the undesired effect of smearing sharp spectral peaks across several adjacent bins and apparently this modifies the source to the extent that the resulting acoustic field is grossly in error.

A technique which removes the unresolved low-frequency components instead of folding their energy into the nearby frequency bins is desirable. The technique should have as little effect on the sharp spectral features (i.e. the periodic components) as possible. One common method for accomplishing this is to subtract any linear trend between the first and last† data points of the signal before performing the transform. Obviously if the frequency of the unresolved energy is low enough that it can be represented as a linear function over the period of the transform then the unresolved energy is removed. If the signal consists of a superposition of periodic components and aperiodic components then this method has no effect on the periodic components.

Moreover, the data can first be segmented into a number of (possibly) overlapping segments, and a linear trend can be subtracted between the first and last points of each segment. The transforms of the individual segments are subsequently averaged together. Again, this technique has no effect on the components of the signal that are periodic over the segment length. However, the energy contained in components of the signal that not exactly resolved on the length of a segment is attenuated by the subtraction of the linear trends. Since the lowest frequency to resolve is $f/8$ a transform of length at least $8T$ is needed. This corresponds to 128 samples. The efficacy of this modified DFT technique in removing spurious low-frequency noise components added to a periodic signal is shown by example in Colonius *et al.* (1995). Its efficacy in transforming the acoustic sources is shown below. Given the segment length of 128 (a period of $8T$) samples and the total length of the signal 1024 samples (a period of $64T$), the only parameter left to choose is the amount of overlap of each segment. It is shown in Colonius *et al.* (1995) that for spurious low frequencies ($0 < \omega < f/8$) overlapping the segments by all but 1 point is the best choice.

In summary, the modified DFT procedure is defined by

$$\hat{F}_n = \frac{1}{Mp'} \sum_{p=0}^{p'} \sum_{j=j'}^{j'+M-1} \left(F(t_j) - \frac{(j-j')(F(t_{j'+M}) - F(t_{j'}))}{M} \right) \mathrm{e}^{-2\pi i n j/M}, \tag{A 2}$$

where $j' = p(M-R)$, $p' = \text{Integer}(N-M)/(M-R)$, n is the integer frequency, N is the total number of samples, M is the segment length, and R is the amount of overlap in successive segments. The predictions given in §3 rely on sources which were transformed according to equation (A 2).

The efficacy of this approach for transforming the sources is now demonstrated. In figure 21, the magnitude of the total source term (equation (3)) and the resulting prediction for the acoustic field are given for three different cases: (*a*) the standard DFT (equation (A 1)) is used with 1024 samples over the 64 periods of the fundamental frequency; (*b*) the modified DFT (equation (A 2)) is used; (*c*) the *difference* between the sources computed in (*b*) and (*a*) is used as the source for the acoustic analogy prediction. Note that the contour levels for the difference in the sources are 20 times smaller than those of (*a*) and (*b*). Differences between the source computed with the different DFT procedures appear to be minor, and arise primarily in the sponge region, and to a much lesser degree in the physical part of the domain downstream of the saturation point of the second subharmonic frequency.

However, these small differences in the source terms computed using different DFT procedures are apparently greatly amplified in solving the acoustic analogy. While the modified DFT gives good agreement with the DNS, the standard DFT procedure

† By 'last point in the data' we mean the point which completes a full period of the data – in terms of equation (9) this point would be labeled t_N.

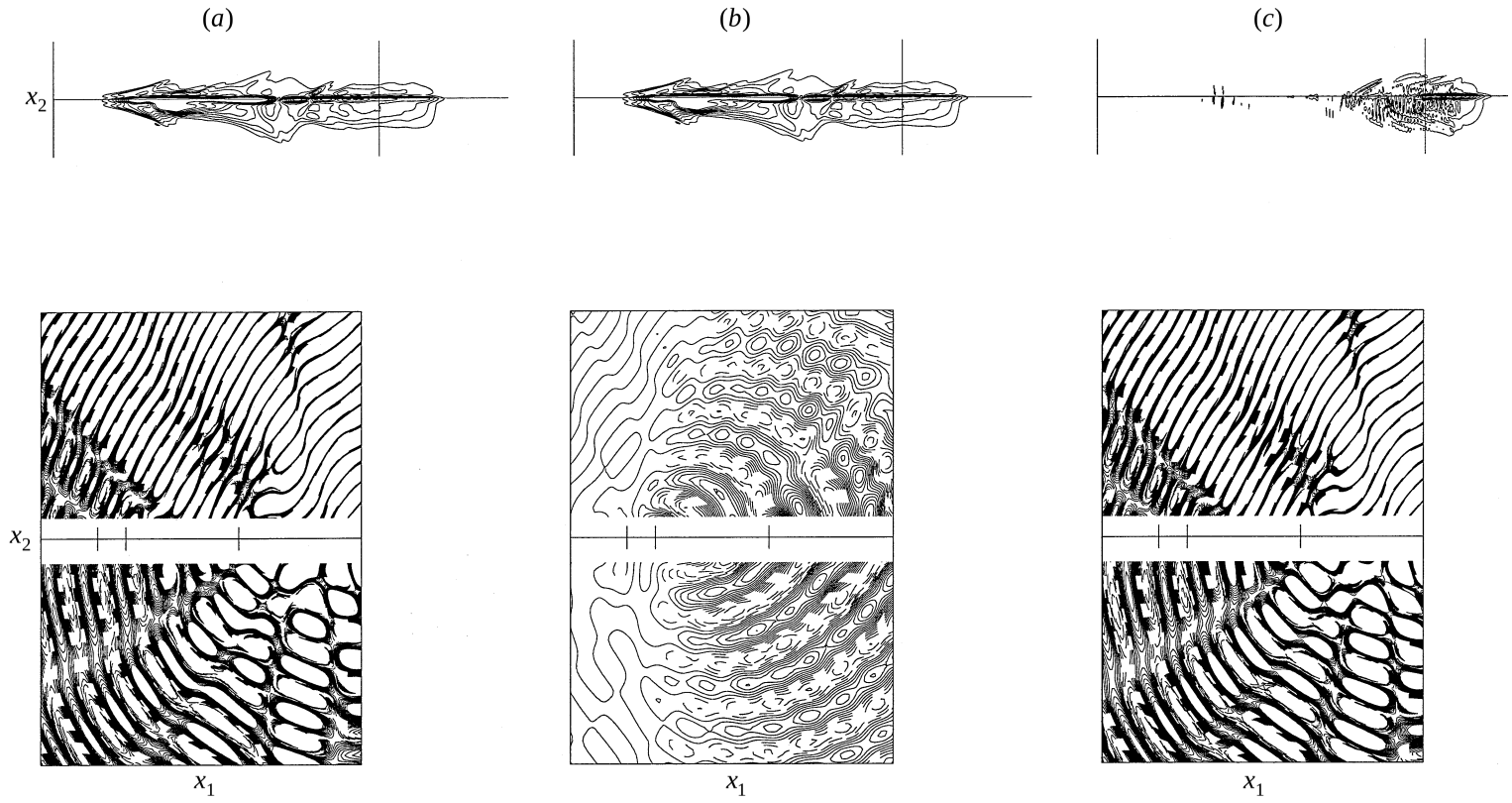

FIGURE 21. The magnitude of the full acoustic source given by equation (3) (top row) and resulting acoustic field (bottom row). The source is computed with (*a*) the standard DFT, (*b*) the modified DFT. The field shown in (*c*) is the *difference* between the sources computed according to (*b*) and (*a*). For the source terms the region shown is the same as shown in figure 13, for the acoustic fields it is the same as shown in figure 5. Contour levels for source terms: (*a*) and (*b*) -1×10^{-4} to 1×10^{-4} at intervals of 0.1×10^{-4}; (*c*) 0.5×10^{-6} to 5×10^{-6} at intervals of 0.5×10^{-6}. Contour levels for all acoustic fields (times 10^6): -0.4 to 0.4 at intervals of 0.04.

gives an acoustic field which is nearly an order of magnitude too large and which, unlike the DNS, appears to emanate primarily from the region downstream of the second pairing and from the sponge. It is also evident that the predictions for cases (*a*) and (*c*) are nearly identical, but opposite in sign. We conclude that the spurious waves emanating downstream of the second pairing in procedure (*a*) are due entirely to the differences in the source terms, which in turn arise from the slightly aperiodic contamination of the DNS signal.

REFERENCES

Balsa, T. F. 1976 The far field of high frequency convected singularities in sheared flows, with an application to a jet-noise prediction. *J. Fluid Mech.* **74**, 193–208.

Balsa, T. F. 1977 The acoustic field of sources in shear flow with application to jet noise: convective amplification. *J. Fluid Mech.* **79**, 33–47.

Bridges, J. & Hussain, F. 1992 Direct evaluation of aeroacoustic theory in a jet. *J. Fluid Mech.* **240**, 469–501.

Brown, G. L. & Roshko, A. 1974 On density effects and large structures in turbulent mixing layers. *J. Fluid Mech.* **64**, 775–816.

Colonius, T., Lele, S. K. & Moin, P. 1993 Boundary conditions for direct computation of aerodynamic sound. *AIAA J.* **31**, 1574–1582; also *DGLR/AIAA Paper* 92-02-075.

Colonius, T., Lele, S. K. & Moin, P. 1994 The scattering of sound waves by a vortex – numerical simulations and analytical solutions. *J. Fluid Mech.* **260**, 271–298.

Colonius, T., Lele, S. K. & Moin, P. 1995 Direct computation of aerodynamic sound. *Rep.* TF-65. Thermoscience Division, Department of Mechanical Engineering, Stanford University.

Crighton, D. G. 1986 Goals for computational aeroacoustics. In *Computational Acoustics: Algorithms and Applications. Proc. 1st IMACS Symp. on Computational Acoustics, New Haven, CT.*

Crighton, D. G. 1993 Computational aeroacoustics for low Mach number flows. In *Computational Aeroacoustics* (ed. J. C Hardin & M. Y. Hussaini), pp. 50–68. Springer.

Crighton, D. G. & Huerre, P. 1990 Shear-layer pressure fluctuations and superdirective acoustic sources. *J. Fluid Mech.* **220**, 355–368 (referred to herein as CH).

Crow, S. C. 1970 Aerodynamic sound emission as a singular perturbation problem. *Stud. Appl. Maths* **49**, 21–44.

Doak, P. E. 1972 Analysis of internally generated sound in continuous materials: 2. A critical review of the conceptual adequacy and physical scope of existing theories of aerodynamic noise, with special reference to supersonic jet noise. *J. Sound Vib.* **25**, 263–335.

Dowling, A. P., Ffowcs Williams, J. E. & GOLDSTEIN, M .E. 1978 Sound production in a moving stream. *Phil. Trans. R. Soc. Lond.* A **288**, 321–349.

Ffowcs Williams, J. E. 1974 Sound production at the edge of a steady flow. *J. Fluid Mech.* **66**, 791–816.

Freund, J. B., Lele, S. K. & Moin, P. 1995 Calculation of the radiated sound field using an open Kirchhoff surface. *CEAS/AIAA Paper* 95-061.

Giles, M. B. 1990 Non-reflecting boundary conditions for Euler equation calculations. *AIAA J.* **28**, 2050–2058.

Givoli, D. 1991 Non-reflecting boundary conditions. *J. Comput. Phys.* **94**, 1–29.

Goldstein, M. E. 1975 The low frequency sound from multipole sources in axisymmetric shear flows, with applications to jet noise. *J. Fluid Mech.* **70**, 595–604.

Goldstien, M. E. 1976*a* *Aeroacoustics.* McGraw-Hill.

Goldstein, M. E. 1976*b* The low frequency sound from multipole sources in axisymmetric shear flows. Part 2. *J. Fluid Mech.* **75**, 17–28.

Goldstein, M. E. 1982 High frequency sound emission from moving point multipole sources embedded in arbitrary transversely sheared mean flows. *J. Sound Vib.* **80**, 499–522.

Goldstein, M. E. 1984 Aeroacoustics of turbulent shear flows. *Ann. Rev. Fluid Mech.* **16**, 263–285.

Gottlieb, J. J. 1960 Sound sources near a velocity discontinuity. *J. Acoust. Soc. Am.* **32**, 1117–1122.

HUERRE, P. & CRIGHTON, D. G. 1983 Sound generation by instability waves in a low Mach number jet. *AIAA Paper* 83-0661.

KIBENS, V. 1980 Discrete noise spectrum generated by an acoustically excited jet. *AIAA J.* **18**, 434–441.

LAUFER, J. & YEN, T. 1983 Noise generation by a low-Mach-number jet. *J. Fluid Mech.* **134**, 1–31.

LELE, S. K. 1992 Compact finite difference schemes with spectral-like resolution. *J. Comput. Phys.* **103**, 16–42.

LIGHTHILL, M. J. 1952 On sound generated aerodynamically: I.– General theory. *Proc. R. Soc. Lond.* A **211**, 654–587.

LIGHTHILL, M. J. 1954 On sound generated aerodynamically: II. – Turbulence as a source of sound. *Proc. R. Soc. Lond.* A **222**, 1–32.

LIGHTHILL, M. J. 1992 Report on the final panel discussion on computational aeroacoustics. *ICASE Rep.* 92-53.

LILLEY, G. M. 1974 On the noise from jets. *AGARD CP*-131.

LYRINTZIS, A. S. 1993 The use of Kirchhoff's method in computational aeroacoustics. *Computational Aero and Hydro Acoustics.* ASME Fluids Engineering Division, Vol. 147, pp. 53–62.

MANI, R. 1976 The influence of jet flow on jet noise. Part 1. The noise of unheated jets. *J. Fluid Mech.* **73**, 753–778.

MANKBADI, R. R. 1990 The self-noise from ordered structures in a low Mach number jet. *Trans. ASME* E: *J. Appl. Mech.* **157**, 241–246.

MANKBADI, R. & LIU, J. T. C. 1984 Sound generated aerodynamically revisited: Large scale structures in a turbulent jet as a source of sound. *Phil. Trans. R. Soc. Lond.* A **311**, 183–217.

MITCHELL, B. E. & LELE, S. K. & MOIN, P. 1995 Direct computation of the sound from a compressible co-rotating vortex pair. *J. Fluid Mech.* **285**, 181–202.

MITCHELL, B. E. & LELE, S. K. & MOIN, P. 1996 Direct computation of the sound generated by subsonic and supersonic axisymmetric jets. *Rep.* TF-66. Thermoscience Division, Department of Mechanical Engineering, Stanford University.

PRESS, W., FLANNERY, B., TEUKOLSKU, S. & VETTERLING, W. 1992 *Numerical Recipes. The Art of Scientific Computing*, 2nd Edn. Cambridge University Press.

SANDHAM, N. D. & REYNOLDS, W. C. 1989 A numerical investigation of the compressible mixing layer. *Rep.* TF-45.Thermosciences Division, Department of Mechanical Engineering, Stanford University.

SARKAR, S. & HUSSAINI, M. K. 1993 Computation of the sound generated by isotropic turbulence. *ICASE Rep.* 93-74.

TAM, C. K. W. 1995 Supersonic jet noise. *Ann. Rev. Fluid Mech.* **27**, 17–43.

TAM, C. K. W. & MORRIS, P. J. 1980 The radiation of sound by the instability waves of a compressible plane turbulent shear layer. *J. Fluid Mech.* **98**, 349–381.

TESTER, B. J. & BURRIN, R. H. 1974 On sound radiation from sources in parallel sheared jet flows. *AIAA Paper* 74-57.

TESTER, B. J. & MORFREY, C. L. 1976 Developments in jet noise modeling–theoretical predictions and comparisons with measured data. *J. Sound Vib.* **46**, 79–103.